

# Super $B$ Detector Technical Design Report

## Abstract

This report describes the technical design detector for Super $B$ .



# Contents

<b>1</b>	<b>Introduction</b>	<b>1</b>
1.1	The Physics Motivation . . . . .	1
1.2	The SuperB Project Elements . . . . .	1
1.3	The Detector Design Progress Report . . . . .	2
<b>2</b>	<b>Accelerator Overview</b>	<b>5</b>
<b>3</b>	<b>Detector Overview</b>	<b>7</b>
3.1	Physics Performance . . . . .	7
3.2	Challenges on Detector Design . . . . .	10
3.3	Open Issues . . . . .	12
3.4	Detector R&D . . . . .	12
<b>4</b>	<b>Physics with SuperB</b>	<b>17</b>
<b>5</b>	<b>Machine Detector Interface and Backgrounds</b>	<b>19</b>
<b>6</b>	<b>Silicon Vertex Tracker</b>	<b>21</b>
6.1	Vertex Detector Overview	G.Rizzo - 12 pages . . . . . 21
6.2	Backgrounds	R.Cenci - 4 pages . . . . . 21
6.3	Detectors Performance Studies	N.Neri - 6 pages . . . . . 21
6.4	Silicon Sensors	L. Bosisio - 8 pages . . . . . 21
6.5	Fanout Circuits	L.Vitale - 8 pages . . . . . 21
6.6	Electronics Readout	28 pages . . . . . 21
6.6.1	Readout chips	V.Re - 10 . . . . . 21
6.6.2	Hybrid Design	M.Citterio - 10 . . . . . 21
6.6.3	Data Transmission	M.Citterio - 10 . . . . . 21
6.6.4	Power Supply	- 2 . . . . . 21
6.7	Mechanical Support & Assembly	S.Bettarini/F.Bosi - 14 pages . . . . . 21
6.8	Layer0 Upgrade Options	G.Rizzo/L.Ratti - 10 pages . . . . . 21
6.9	Services, Utilities	- 8 pages . . . . . 21
<b>7</b>	<b>Drift Chamber</b>	<b>- Finocchiaro, Roney 60 pages 25</b>
7.1	Overview	- Finocchiaro, Roney 12 pages . . . . . 25
7.1.1	Physics requirements	- 3 pages . . . . . 25
7.1.2	Geometrical constraints	- 1 page . . . . . 25
7.1.3	Machine background considerations	- 2 pages . . . . . 25
7.1.4	DCH design overview	- 2 pages . . . . . 25
7.1.5	Expected performance	- 2 pages . . . . . 25
7.1.6	Tracking software and pattern recognition	- 2 pages . . . . . 25

7.2	Optimization of chamber operation	- Finocchiario, Hearty, Piccolo, Roney 9 pages	25
7.2.1	Prototype studies		25
7.2.2	Gas Mixture Optimization		25
7.2.2.1	Physics performance considerations		25
7.2.2.2	Aging studies: fields, gas gain		25
7.2.3	Cluster Counting		25
7.3	Mechanical Design	- Finocchiario, Lauciani 9 pages	25
7.3.1	Endplates		25
7.3.2	Inner cylinder		25
7.3.3	Outer Cylinder		25
7.3.4	Cell structure		25
7.3.5	Choice of wire and electrostatic stability		25
7.3.6	Feed-through design		25
7.3.7	Endplate system		25
7.3.7.1	Supports for on-detector boards		25
7.3.7.2	Cooling		25
7.3.7.3	Shielding		25
7.3.8	Stringing		25
7.4	Electronics	- Felici, Martin 12 pages	25
7.4.1	Design Goals		25
7.4.1.1	Specifications for charge measurements		25
7.4.1.2	Specifications for time measurements		25
7.4.2	DCH Front-end system (block diagram)		25
7.4.3	On-detector electronics		25
7.4.3.1	Preamplifier		25
7.4.3.2	Cabling		25
7.4.4	Off-detector electronics		25
7.4.4.1	Triggered data path		25
7.4.4.2	Non-triggered data path		25
7.4.5	Optical Links		26
7.4.5.1	Patch panels		26
7.5	High Voltage system	- Martin 1 page	26
7.5.1	Main HV system		26
7.5.2	Distribution boards		26
7.6	Gas system	- Roney 2 pages	26
7.7	Calibration and monitoring	- Roney 3 pages	26
7.7.0.1	Slow control systems		26
7.7.0.2	Calibration		26
7.7.0.3	Gas monitoring system		26
7.7.0.4	On-line monitor		26
7.8	Integration	- Hearty, Lauciani 6 pages	26
7.8.1	Overall geometry and mechanical support		26
7.8.2	Cable supports and routing		26
7.8.3	Access		26
7.8.4	Gas system		26
7.8.5	Off-detector electronics crates		26
7.8.6	High voltage crates		26



7.8.7	Installation and alignment	26
7.9	R&D Program - Finocchiaro, Piccolo 6 pages	26
7.9.1	Results	26
7.9.2	Plans	26
<b>8</b>	<b>Particle Identification</b>	<b>29</b>
8.1	Summary of Physics Requirements and Detector Performance goals 3-4 pages	29
8.1.1	Physics requirements Cincinnati, Maryland	29
8.1.2	Detector concept	29
8.1.3	Charged Particle Identification	30
8.2	Particle Identification Overview 2-3 pages	30
8.2.1	Experience of BaBar DIRC	30
8.2.2	Barrel PID: Focusing DIRC (FDIRC)	31
8.3	Projected Performance of FDIRC 2-3 pages	34
8.3.1	Reconstruction Arnaud, Roberts	34
8.3.2	MC Simulation	34
8.3.3	Effect of Background on performance Cenci, Vavra, Kravchenko	34
8.4	The Barrel FDIRC Detector Overview 5-10 pages	34
8.4.1	Impact on other systems Benettoni, Simi, Vavra	35
8.4.2	Photodetectors	35
8.4.3	Laser calibration system	43
8.4.4	FDIRC Mechanical Design 5 pages	43
8.4.5	Mechanical support	43
8.4.6	Electronics readout, HV and LV 5-6 pages	46
8.4.7	Integration issues 2 pages	46
8.4.8	DAQ and computing 1 page	46
8.4.9	FDIRC R&D Results until now 2-3 pages	46
8.4.10	Ongoing FDIRC R&D 1-2 pages	47
8.4.11	System Responsibilities and Management 1-2 pages	47
8.4.12	Cost, Schedule and Funding Profile 1-2 pages	47
8.5	Forward option 4-5 pages	47
8.5.1	Physics motivation Arnaud, Stocchi	47
8.5.2	Outline of FTOF detector technology Arnaud, Stocchi, Vavra	47
8.5.3	Committee recommendation Hassan	47
8.5.4	Motivation for a Forward PID Detector	47
8.5.5	Forward PID Requirements	47
8.5.6	Status of the Forward PID R&D Effort	48
<b>9</b>	<b>Electromagnetic Calorimeter</b>	<b>53</b>
9.1	Overview	53
9.1.1	Background and radiation issues	53
9.1.2	Simulation tools	55
9.1.2.1	Fastsim	55
9.1.2.2	Full sim	55
9.2	Barrel Calorimeter	55
9.2.1	Requirements Relevant to the SuperB Environment	56
9.2.1.1	Crystal Aging at BABAR	56
9.2.1.2	Backgrounds	56

9.2.2	Description of <i>BABAR</i> Barrel Calorimeter . . . . .	56
9.2.2.1	Mechanical design . . . . .	56
9.2.2.2	Readout . . . . .	56
9.2.2.3	Calibration . . . . .	56
9.2.3	Performance of <i>BABAR</i> barrel . . . . .	56
9.2.3.1	Energy and position resolution . . . . .	56
9.2.3.2	Gamma-gamma mass resolution . . . . .	56
9.2.3.3	Radiation Damage Effects on Resolution . . . . .	56
9.2.3.4	Expected Changes in Performance at <i>SuperB</i> . . . . .	56
9.2.4	Electronics changes . . . . .	56
9.2.4.1	Rationale for changes . . . . .	56
9.2.4.2	Premp design . . . . .	56
9.2.4.3	Shaping and digitization . . . . .	56
9.2.4.4	Cabling . . . . .	56
9.2.5	SLAC De-installation, Transport and Local Storage . . . . .	56
9.2.6	Electronics refurbishment . . . . .	56
9.2.7	Calibration systems . . . . .	56
9.2.8	Re-installation at Tor Vergata . . . . .	56
9.3	Forward Calorimeter . . . . .	56
9.3.1	Requirements[RF] . . . . .	56
9.3.2	LYSO Crystals[RZ] . . . . .	57
9.3.2.1	Light output . . . . .	57
9.3.2.2	Radiation hardness . . . . .	57
9.3.2.3	Timing . . . . .	57
9.3.2.4	Uniformity . . . . .	57
9.3.2.5	Manufacturing . . . . .	57
9.3.3	Readout and Electronics[VB] . . . . .	57
9.3.3.1	APD Readout[DH] . . . . .	57
9.3.3.2	Electronics Block diagram . . . . .	57
9.3.3.3	Preamplifier . . . . .	57
9.3.3.4	Shaper . . . . .	57
9.3.3.5	Digitization . . . . .	57
9.3.3.6	Requirements on mechanics . . . . .	57
9.3.4	Calibration[DH] . . . . .	57
9.3.4.1	Initial calibration with source . . . . .	57
9.3.4.2	6 MeV calibration system . . . . .	57
9.3.4.3	Electronics calibration . . . . .	57
9.3.4.4	Temperature monitoring and correction . . . . .	57
9.3.5	Mechanical Design[CG] . . . . .	57
9.3.5.1	Introduction and parameters . . . . .	57
9.3.5.2	General constraints and requirements . . . . .	57
9.3.5.3	Cooling and Calibration requirements . . . . .	59
9.3.5.4	Crystal sub-unit design . . . . .	59
9.3.5.5	Module design . . . . .	61
9.3.5.6	Alveolar module structure finite element analysis . . . . .	65
9.3.5.7	Support shell structure design . . . . .	68
9.3.5.8	Global structure finite element analysis . . . . .	68

9.3.6	Performance in simulations[SG]	68
9.3.6.1	Resolution studies	68
9.3.6.2	Background studies	68
9.3.7	Tests on Beam[CC]	68
9.3.7.1	Description of apparatus	68
9.3.7.2	Electronics noise measurements	69
9.3.7.3	Description of beam	73
9.3.7.4	Description of data	75
9.3.7.5	Calibration	75
9.3.7.6	Data-MC comparison	75
9.3.7.7	Temperature corrections	77
9.3.7.8	Algorithms and results	77
9.3.8	Alternatives	77
9.3.8.1	Alternative 1	77
9.3.8.2	Comparison with baseline	77
9.4	Backward Calorimeter	78
9.4.1	Improvements on physics results	78
9.4.2	Requirements	79
9.4.2.1	Energy and angular resolution	79
9.4.2.2	Background rates	79
9.4.2.3	Radiation hardness	80
9.4.2.4	Solid angle, transition to barrel	80
9.4.3	Mechanical design	80
9.4.3.1	Calorimeter construction	81
9.4.3.2	Support and services	81
9.4.4	SiPM/MPPC readout	81
9.4.5	Electronics	81
9.4.6	Calibration	82
9.4.7	Backward simulation	82
9.4.8	Performance in simulations	83
9.4.9	Use for particle identification	84
9.4.10	Discussion of task force conclusions	86
9.5	Trigger	86
9.5.1	Calorimeter readout trigger	86
9.5.1.1	Normal mode	86
9.5.1.2	Calibration mode	86
9.5.2	Calorimeter trigger primitives	86
9.6	Detector protection	86
9.6.1	Thermal shock	86
9.6.2	Mechanical shock, including earthquakes	86
9.6.3	Fluid spills	86
9.6.4	Electrical surges, outages	86
9.6.5	Radiation damage	86
9.7	Cost & Schedule	86
9.7.1	WBS structure	86
9.7.2	Gantt chart	86
9.7.3	Basis of estimates	86

9.7.4	Cost and schedule risks	86
9.8	Barrel Calorimeter	87
9.9	Forward Endcap Calorimeter	88
9.9.1	Mechanical Structure	88
9.9.2	Readout System	89
9.9.3	Calibration and Beam Test	89
9.9.4	Performance Studies	89
9.10	Backward Endcap Calorimeter	90
9.11	R&D	92
9.11.1	Barrel Calorimeter	92
9.11.2	Forward Calorimeter	93
9.11.3	Backward Calorimeter	93
<b>10</b>	<b>Instrumented Flux Return</b>	<b>75</b>
10.1	Performance Optimization	75
10.1.1	Identification Technique	75
10.1.2	Baseline Design Requirements	76
10.1.3	Design Optimization and Performance Studies	76
10.2	R&D Work	77
10.2.1	R&D Tests and Results	77
10.2.2	Prototype	78
10.3	Baseline Detector Design	79
10.3.1	Flux Return	79
<b>11</b>	<b>Magnet and Flux Return</b>	<b>83</b>
<b>12</b>	<b>Trigger, DAQ and Online</b>	<b>85</b>
12.1	Overview of the Architecture	85
12.1.1	Trigger Strategy	85
12.1.2	Trigger Rates and Event Size Estimation	86
12.1.3	Dead Time and Buffer Queue Depth Considerations	87
12.2	Electronics, Trigger and DAQ	87
12.2.1	Fast Control and Timing System	87
12.2.2	Clock, Control and Data Links	89
12.2.3	Common Front-End Electronics	90
12.2.4	Readout Module	90
12.2.5	Experiment Control System	91
12.2.6	Level 1 Hardware Trigger	92
12.3	Online System	93
12.3.1	ROM Readout and Event Building	93
12.3.2	High Level Trigger Farm	93
12.3.3	Data Logging	94
12.3.4	Event Data Quality Monitoring and Display	94
12.3.5	Run Control System	94
12.3.6	Detector Control System	94
12.3.7	Other Components	95
12.3.8	Software Infrastructure	95

12.4	Front-End Electronics	95
12.4.1	SVT Electronics	95
12.4.2	DCH Electronics:	96
12.4.3	PID Electronics:	97
12.4.4	EMC Electronics:	98
12.4.5	IFR Electronics:	99
12.5	R&D	100
12.6	Conclusions	101
<b>13</b>	<b>Electronics</b>	<b>105</b>
13.1	Electronics overview	105
13.2	Common components	105
13.2.1	FCTS Links	105
13.2.2	Data Links	105
13.2.3	Common Front-End Electronics (CFEE)	105
13.2.4	Power supplies (?)	105
13.2.5	Cable Plant (?)	105
13.3	Subsystem-specific Electronics	105
13.3.1	SVT	105
13.3.2	DCH	105
13.3.3	PID	105
13.3.4	EMC	105
13.3.5	IFR	105
13.3.6	Trigger	105
<b>14</b>	<b>Software and Computing</b>	<b>107</b>
14.1	The Super <i>B</i> baseline model	107
14.1.1	The requirements	108
14.1.2	Super <i>B</i> offline computing development	109
14.2	Computing tools and services for the Detector and Physics TDR studies	109
14.2.1	Fast simulation	109
14.2.2	Bruno: the Super <i>B</i> full simulation tool	112
14.2.3	The distributed production environment	113
14.2.4	The software development and collaborative tools	116
14.2.5	Code packaging and distribution	117
<b>15</b>	<b>Environmental Safety and Health</b>	<b>121</b>
<b>16</b>	<b>Facilities, Mechanical Integration and Assembly</b>	<b>123</b>
16.1	Introduction	123
16.1.1	Magnet and Instrumented Flux Return	123
16.2	Component Extraction	124
16.3	Component Transport	125
16.4	Detector Assembly	126
<b>17</b>	<b>Project Management</b>	<b>127</b>

<b>18 Cost and Schedule</b>	<b>129</b>
18.1 Detector Costs . . . . .	130
18.2 Basis of Estimate . . . . .	134
18.3 Schedule . . . . .	135

# 9 Electromagnetic Calorimeter

## 9.1 Overview

---

Calorimetry at SuperB is achieved with three major components: A CsI(Tl) “barrel” calorimeter covering the central region, a LYSO(Ce) “forward” calorimeter covering the small angle region in the direction of the high energy beam, and a lead-scintillator “backward” calorimeter covering the small angle region in the direction of the low energy beam. Table 9.1 shows the solid angle coverage for each of the three parts of the SuperB EMC. The superB electromagnetic calorimeter (EMC) will play an essential role in the study of the flavor physics especially in the sector in which  $B$  meson decays involve neutral particles. The calorimeter provides energy and direction measurement of photons and electrons, reconstruction of neutral hadrons such as  $\pi^0$ 's and discrimination between electrons and charged hadrons. Many channels containing missing energy due to the presence of neutrinos will rely on information from the EMC to discriminate against backgrounds.

The SuperB EMC reuses the barrel part of the BaBar EMC detector consisting of 5760 CsI(Tl) crystals as shown in Fig. ?? . However the BABAR forward calorimeter will need to be replaced, due to the higher radiation and higher rates at SuperB compared with PEP-II. The forward endcap will be replaced by a new scintillating crystal calorimeter designed to work well in this new environment. Compared with the BaBar calorimeter where good energy and position resolution are required, the same criteria apply for SuperB. After an intensive R&D program the baseline option for the SuperB forward calorimeter is to use the faster and more radiation resistant LYSO crystals. As will be discussed below, this is the clear favorite

in terms of performance and radiation hardness over the alternatives we have considered. The faster response time and shorter Molière radius serve together to address the higher event and background rates. LYSO is a fast scintillator largely used in medical applications with crystals of small size. The R&D was concentrated on the optimization of performance for large crystals (2cm x 2 cm x 20 cm) with good light yield uniformity and optimized Ce doping in order to have the best possible light output. Thanks to this effort, more than one producer is able to grow LYSO crystals of good quality that can be used in high energy physics applications. Table ?? shows the comparison between LYSO and other materials used in electromagnetic calorimeters. The largest disadvantage of LYSO is cost, and we have studied lower cost alternatives as described below.

Finally, a lead-scintillator-sandwich backward endcap calorimeter improves the hermeticity of the detector. The main purpose of this component is to detect energy in the backward endcap region, as a veto of with extra “extra” energy. This is particularly important for studying channels with neutrinos in the final state. Because of the fast time response, the backward EMC may also have a role in particle identification by providing time-of-flight for the relatively slow backward-going charged particles.

### 9.1.1 Background and radiation issues

One of the major concerns for the electromagnetic calorimeter is its capability to sustain the radiation dose, dose which is larger than in previous experiments due to the increased luminosity. The dominant contribution to radiation in SuperB is in fact expected to come from radiative bhabha events, that emit a large number of low energy photons at an extremely high rate. This photon rate can impact the performances

Table 9.1: Solid angle coverage of the electromagnetic calorimeters. Values are obtained assuming the barrel calorimeter is in the same location with respect to the collision point as for *BABAR*. The CM numbers are for massless particles and nominal 4 on 7 GeV beam energies. The barrel Super*B* row includes one additional ring of crystals over *BABAR*.

Calorimeter	$\cos \theta$ (lab)		$\cos \theta$ (CM)		$\Omega$ (CM)(%)
	minimum	maximum	minimum	maximum	
Backward	-0.974	-0.869	-0.985	-0.922	3.1
Barrel ( <i>BABAR</i> )	-0.786	0.893	-0.870	0.824	84.7
Barrel (Super <i>B</i> )	-0.805	0.893	-0.882	0.824	85.2
Forward	0.896	0.965	0.829	0.941	5.6

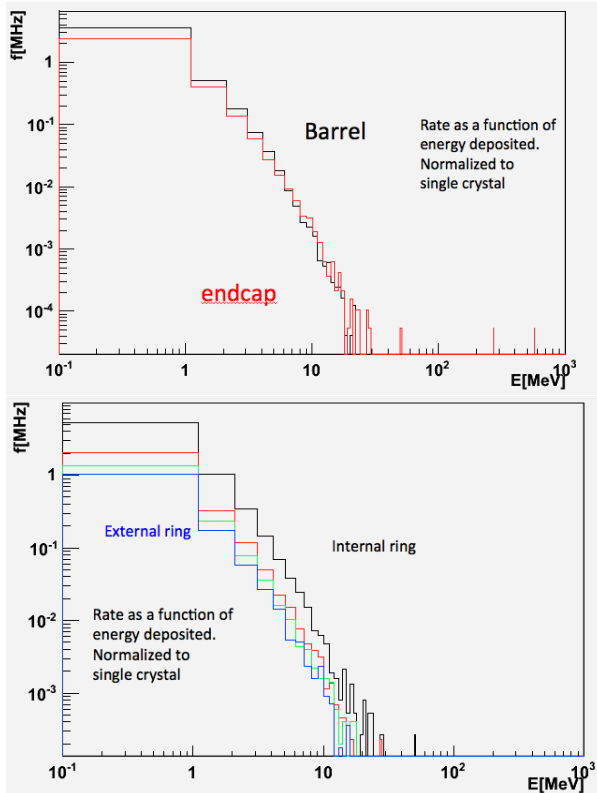


Figure 9.1: Machine Background rates per crystal as a function of deposited energy.

of the detector because of two effects: the radiation can reduce the transmittance of the crystals and therefore alter as a function of time the calibration of the detector; the large number of photons can pile-up with the other effects thus introducing a degradation in energy resolution.

To estimate the impact of these effect a full simulation has been setup as described in Sec. **WHICH SECTION?**. The simulation outputs the energy deposited by radiative Bhabha events in the individual crystals at each beam crossing. i.e. every 2.1ns. This can be converted in terms of rate of photons of a given energy impacting each crystal. The result is shown in Fig. 9.1, both (left) averaging over the whole Barrel and the whole FWD and (right) averaging over the rings of the FWD which have the same number of crystals per ring. The result shows that there is no significant difference in the irradiation between the Barrel and the Endcap. This can be understood because the dimension of the crystals is significantly different: due the different density and consequently molier radius, the transverse dimensions of LYSO or BGO crystals are two times smaller than the CsI crystals (both doped and not) and the overall volume of a LYSO or BGO crystal is 6.7 times smaller ( $120\text{cm}^3$  vs  $800\text{cm}^3$ ) than the CsI ones. Since the rates of signals from the machine background scales linearly with volume, the most forward crystals of the Barrel will suffer a background more than six times larger than the more central crystals of the FWD calorimeter, albeit contiguous.

On average therefore each crystal (both of Barrel or Endcap) will see 1MHz of photons between 1 and 5 MeV and 10 KHz of photons between 5-10 MeV. A plausible linear extrapolation in log-log scale would lead to 100Hz between 10-50 MeV and 1Hz between 50-100 MeV.



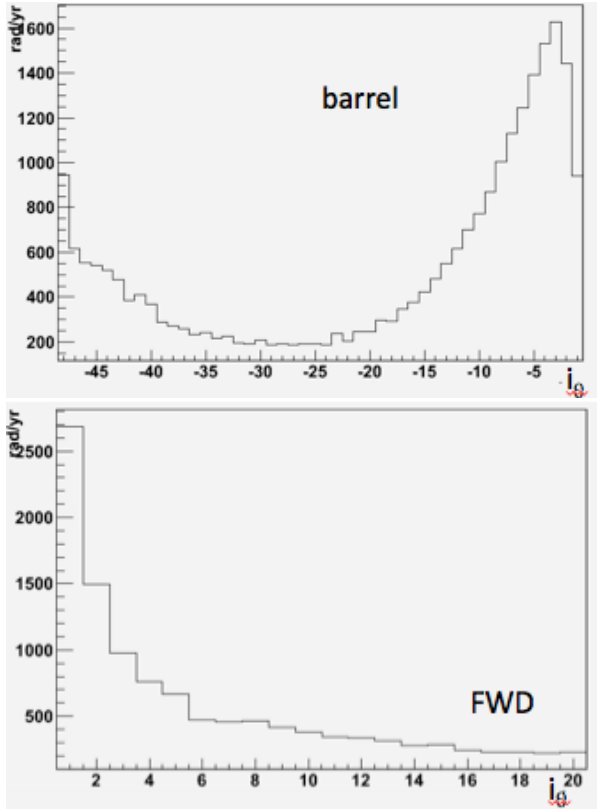


Figure 9.3: Integrated dose as a function of  $i_\theta$  for the Barrel (Left) and FWD (Right) EMC.

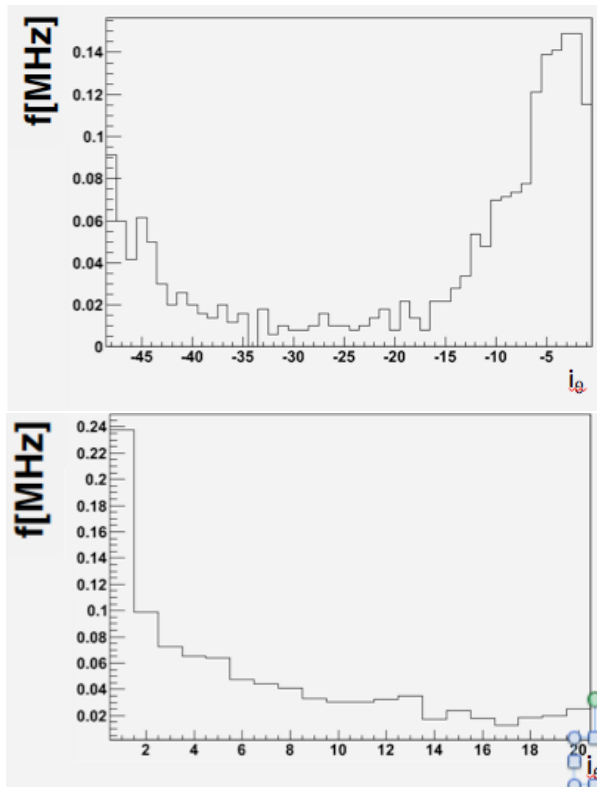


Figure 9.2: Integrated rates for  $E > 5\text{MeV}$  as a function of  $i_\theta$  for the Barrel (Left) and FWD (Right) EMC.

The ring-by-ring details are shown in Fig. 9.2, where the integrated rate of deposits larger than 5MeV are estimated as a function of an index,  $i_\theta$  which is  $i_\theta < -49$  for the backward calorimeter,  $-49 \leq i_\theta < 0$  for the barrel ( $i_\theta = -1$  corresponding to the most forward ring), and  $i_\theta > 0$  for the FWD EMC ( $i_\theta = 1$  corresponding to the innermost ring). It can be noted that the forward region of the barrel ( $i_\theta > -10$ ) is more irradiated than the FWD calorimeter, a part from the innermost ring which is a factor two worse than any other ring.

From the radiation hardness point of view, the dose to which the crystals are sensitive is defined as the total energy deposited in a crystal divided by its mass. The dose expected per year (conventionally considered  $10^7\text{s}$  long) and per crystal is shown in Fig 9.3 separately for the Barrel and the FWD. Conservatively, assuming a maximum of 10 years of operations, crystals need to be radiation resistant up to at least 30krad. Also the impact on resolution of a  $\sim 1\text{rad/hour}$  dose rate needs to be considered.

## 9.1.2 Simulation tools

### 9.1.2.1 Fastsim

### 9.1.2.2 Full sim

## 9.2 Barrel Calorimeter

We propose to re-use the barrel portion of the *BABAR* EMC, retaining the fundamental mechanical structures and the 5760 CsI(Tl) crystals and associated pairs of photodiodes mounted on each crystal, along with some modifications required for optimal performance at *SuperB*.

### 9.2.1 Requirements Relevant to the SuperB Environment

#### 9.2.1.1 Crystal Aging at BABAR

Some text

#### 9.2.1.2 Backgrounds

### 9.2.2 Description of BABAR Barrel Calorimeter

#### 9.2.2.1 Mechanical design

#### 9.2.2.2 Readout

#### 9.2.2.3 Calibration

### 9.2.3 Performance of BABAR barrel

#### 9.2.3.1 Energy and position resolution

#### 9.2.3.2 Gamma-gamma mass resolution

#### 9.2.3.3 Radiation Damage Effects on Resolution

#### 9.2.3.4 Expected Changes in Performance at SuperB

### 9.2.4 Electronics changes

#### 9.2.4.1 Rationale for changes

#### 9.2.4.2 Premp design

#### 9.2.4.3 Shaping and digitization

Synopsis, main discussion in electronics chapter(?)

#### 9.2.4.4 Cabling

changes?

### 9.2.5 SLAC De-installation, Transport and Local Storage

### 9.2.6 Electronics refurbishment

Repair crystals with 0/1 working channels

Preamp replacement

ADC board replacement

### 9.2.7 Calibration systems

Replace DT neutron generator

New plumbing from generator to detector

Repair and reconstitute light pulser system

### 9.2.8 Re-installation at Tor Vergata

## 9.3 Forward Calorimeter

---

The Forward Calorimeter is designed to extend the coverage of the electromagnetic calorimeter to low angles, as detailed in Tab. 9.1. To be effective its performances need therefore be comparable with the Barrel Calorimeter. Thus, the design considers a calorimeter made of homogeneous crystals and read-out by compact photodetectors capable of operating in magnetic field.

As detailed in this section, the best option to fulfill the requirements described in Sec. 9.3.1 is to use crystals made of LYSO readout by Avalanche Photo-Diodes (APD). In Sec. 9.3.8 we will nonetheless report the results of the investigations on other types of crystals, in case budget constraints will not allow the baseline option.

### 9.3.1 Requirements[RF]

Taking as benchmark the BaBar detector, the relative energy resolution need be at most 4.3% at 100 MeV and 2.7% at 1 GeV. Also, in order to assure appropriate resolution on the  $\pi^0$  invariant mass and to allow the  $\pi^0 \rightarrow \gamma\gamma$  reconstruction up to sufficiently high energies, a segmentation at least comparable with the BaBar one is needed. Since the transverse crystal size is dictated by the Molier radius of the material, only crystals with a Molier radius at most as large as the CsI(Tl) can be considered. Finally hermeticity is also important, so the requirement on mechanics is that the fraction of particles originating from the interaction point passing through the cracks of the

As already described for the Barrel Calorimeter, the most stringent constraints come from the presence of large background due to the extremely high luminosity. In particular, as described in Sec. 9.1.1, the large rate of low energy photons can create radiation damage on the crystal themselves, thus reducing the light yield, and induce a degradation of the energy resolution due to pile-up.

As shown in Fig. 9.3, the expected dose integrated in a year ranges from  $\sim 200$  rad for the outermost rings to  $\sim 2500$  rad for the innermost ones. Consequently, the dose rate the

crystals need to tolerate ranges from  $\sim 0.1$  rad/s to  $\sim 1.0$  rad/s, respectively.

In order to estimate the effect of the pile-up on the energy resolution, the study described in Sec. 9.2.1.2 has been extended to the Forward Calorimeter. Contrarily to the case of the Barrel where only one crystal type was considered, several possible crystals were considered for the Forward. The considered options differ, for the purposes of this study only by the decay time of the signal ( $\tau_{dec}$ ). For a given crystal, the additional handles are the time constants of the electronics, in our case the shaping time ( $T_{shape}$ ) and the time constant of the integration circuit ( $T_{int}$ ). Tab. 9.2 shows the expected contribution from pile-up to the energy resolution at 100 MeV and 1 GeV. The constraint on the electronic design is therefore that the contribution to the energy resolution needs to be significantly smaller than the design resolutions of 4.3% and 2.7% respectively.

### 9.3.2 LYSO Crystals[RZ]

Beginning with a survey of possible crystals. (Mostly from RPP)

#### 9.3.2.1 Light output

#### 9.3.2.2 Radiation hardness

#### 9.3.2.3 Timing

#### 9.3.2.4 Uniformity

#### 9.3.2.5 Manufacturing

Vendors, capacity

QA process, test stands

crystal wrapping

### 9.3.3 Readout and Electronics[VB]

#### 9.3.3.1 APD Readout[DH]

#### 9.3.3.2 Electronics Block diagram

#### 9.3.3.3 Preamplifier

#### 9.3.3.4 Shaper

#### 9.3.3.5 Digitization

#### 9.3.3.6 Requirements on mechanics

Cables, encumbrances, required cooling, ...

### 9.3.4 Calibration[DH]

#### 9.3.4.1 Initial calibration with source

#### 9.3.4.2 6 MeV calibration system

#### 9.3.4.3 Electronics calibration

#### 9.3.4.4 Temperature monitoring and correction

### 9.3.5 Mechanical Design[CG]

#### 9.3.5.1 Introduction and parameters

The calorimeter is designed to measure with maximum precision the energy deposited by impinging particles into the crystals. All material out of the crystals is unwelcome because it absorbs a fraction of undetected (unmeasured) energy. Material in front (support shell) and between (cell walls) crystals has to be minimized. Building materials with low-Z molecular composition in limited quantities is favored for this reason. The basic physical requirement to the design of this structure is to ensure a nominal distance between crystal faces of 0.4 mm within a module (gap) and a nominal distance between crystal faces across two modules of 0.6 mm (crack)...and a nominal crystal

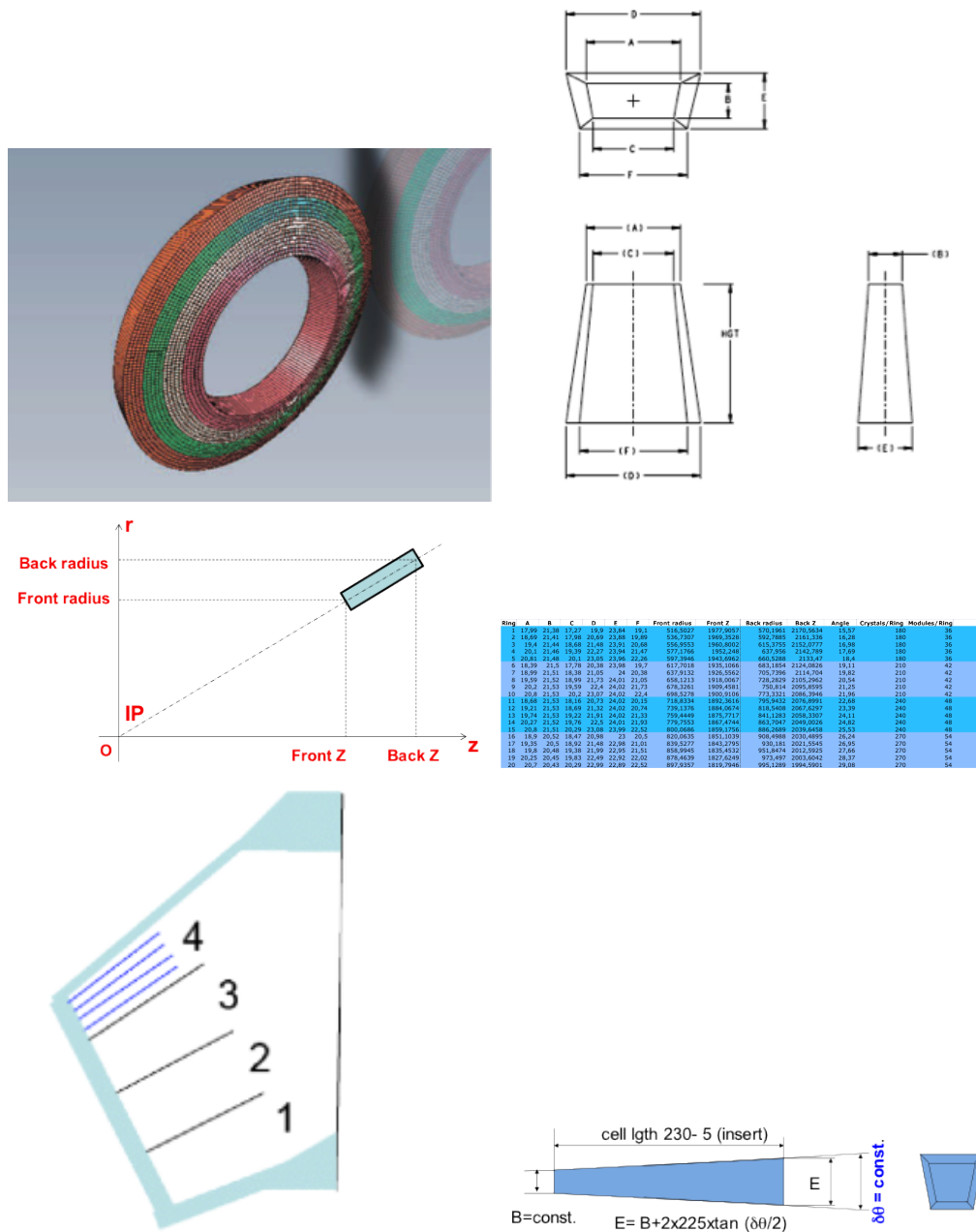
Simmetry in ? Modules 5x5 are displayed in four concentric rings with different numbers of modules. Modules numeber contain common factor 2x3 to simplify deesign and construction: progression from 6 to 9 ring 1: 36= 6x6 modules= 900crystals ring2: 42= 6x7 modules= 1050crystals ring3: 48= 6x8 modules= 1200crystals ring4: 54= 6x9 modules= 1350crystals Simmetry in ? ? division is in four rings, each ring is divided into group of 5 cells.Constant cell front dimension B along ? is maintained.

?

#### 9.3.5.2 General constraints and requirements

from other detctors ... EMC forward volume envelope is the one defined by Babar experiment and reported below. Additional constraints coming from the new requirements for services and access have been considered.

from assembly constraints The design of the mechanical structure foresees that the volume



model	$\tau_{dec}$	$T_{shape}$	$T_{int}$	outermost		innermost	
	(ns)	(ns)	(ns)	100 MeV	1 GeV	100 MeV	1 GeV
LYSO	50	50	??	??	??	??	??
BGO (short)	300	100	??	??	??	??	??
BGO (long)	300	300	??	??	??	??	??
CsI(Tl) (BaBar)	1300	700	??	??	??	??	??
CsI(Tl) (short)	1300	300	??	??	??	??	??

Table 9.2: Contribution to the resolution (in %) induced by machine background on clusters for possible values of  $\tau_{dec}$ ,  $T_{shape}$ , and  $T_{int}$ . The first quote corresponds to an energy of 100 MeV, the second one of 1 GeV. The extreme cases of photons impinging on the outermost or innermost rings of the Forward Calorimeter were considered.

Crystal	LY <sup>1</sup>	$X_0$	$r_M$	Rad	$d(LY)/dT$	$\tau_{decay}$	$\lambda_{max}$
		cm	cm	hard	%/°C	ns	nm
NaI(Tl)	1	2.59	4.13	no	-0.2	230	410
LYSO(Ce)	0.83	1.14	2.07	yes	-0.2	40	402
CsI(Tl)	1.65	1.86	3.57	no	0.3	1300	560
CsI	0.036	1.86	3.57	maybe	-1.3	35	420
BGO	0.21	1.12	2.23	maybe	-0.9	300	480
PbWO <sub>4</sub>	0.0029	0.89	2.00	no	-2.7	10	420

devoted to EMC is divided in two, an alveolar volume and a service volume. The definition of this two volumes is based on assembly constraints and is optimized to simplify access to the services. Volumes shape and dimensions are such to allow free insertion of outer row of crystals

from installation, access and maintenance  
TBD

### 9.3.5.3 Cooling and Calibration requirements

Cooling Structural integrity require any produced heat to be evacuated by a cooling system. The light / signal conversion factor of the photo-detector may depend from the temperature and require a thermal regulation. There are two separate thermal volumes: the volume which encloses the crystals and photodetector, where no power dissipation is expected, and the volume comprised between the modules and the backplate, where all the thermal power is dissipated. The cooling is ensured by two active systems. A regulated circuit keeps the operating temperature of the crystal array and of the photodetec-

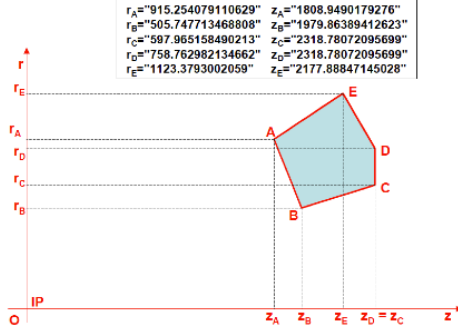
tor within a tight temperature spread (0.XC). A second cooling circuit evacuates the heat generated by all power sources (front-end electronics) in the space between modules and backplate

Calibration A calibration circuit flows a fluid (Fluorinert FC77) activated by a neutron source, 16N decay emits 6,13 MeV ?. The circuit flows past the ECAL front face, thus showering every crystal with calibrated 6,13 MeV ?s, the resulting diode signals are treated by the data acquisition system. Under study either the possibility to reuse the BaBar monitoring system or to build a new circuit embedded in the front sandwich plate of the shell structure.

### 9.3.5.4 Crystal sub-unit design

The crystal subunit consists of the crystal and the capsule assembly with the photo-detector. Upon delivery crystals are visually inspected, measured and characterized. The crystal tolerance ( 0.1 mm), the chamfer width (0.7 mm maximum). Crystal chamfers are necessary to ease surface lapping and polishing, avoid edge chipping and ease safe handling, match cell corner radii. Chamfer size has to be small enough

Measures for the complete BaBar endcap envelop including support structure and electronics (radioactive liquid tubes are not included)



Full ECAL envelope

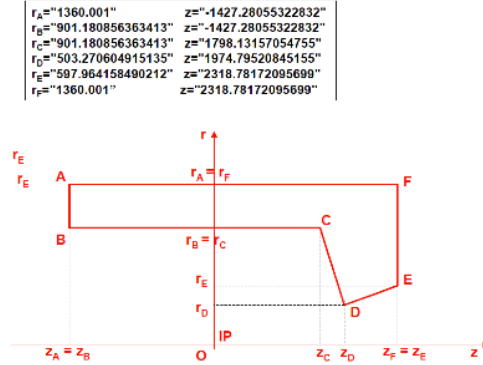


Figure 9.5: crack (crystal to crystal, left picture) and gap (module to module, right picture).

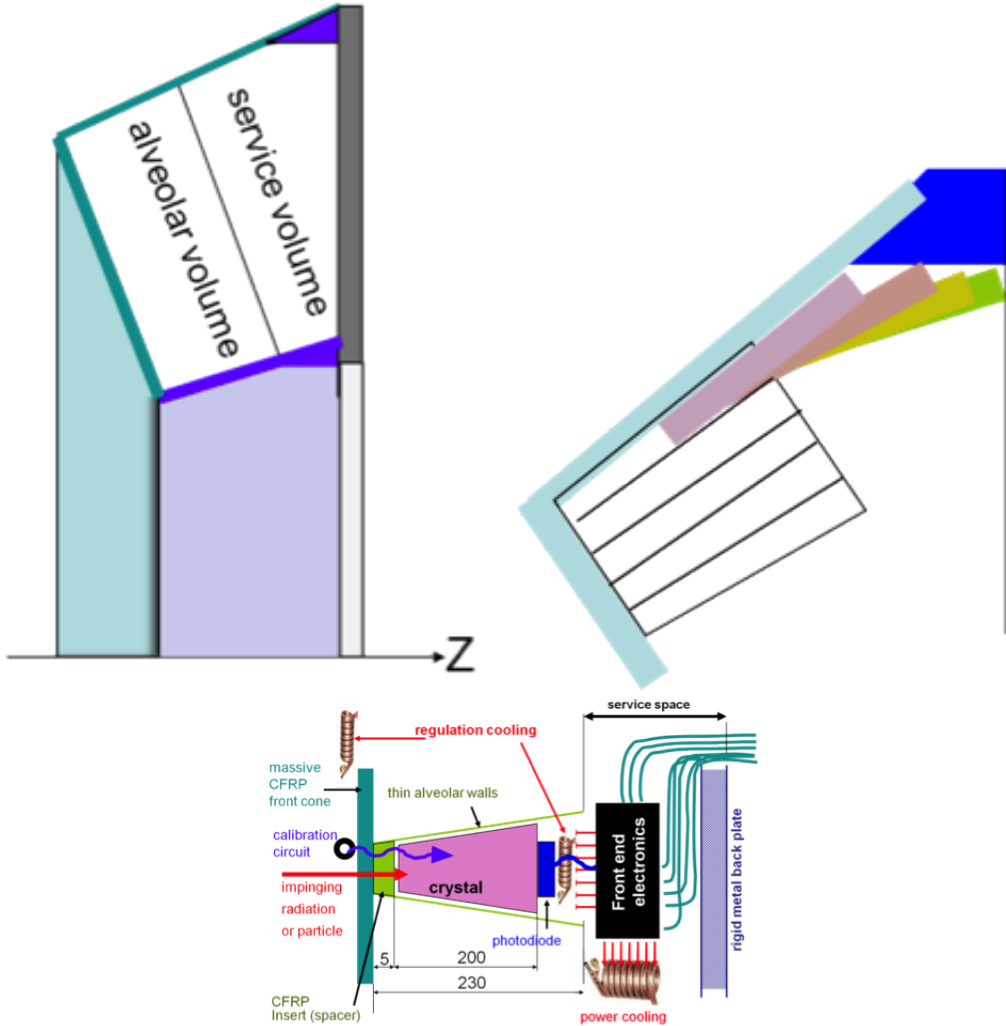


Figure 9.6: emc forward volumes and layout



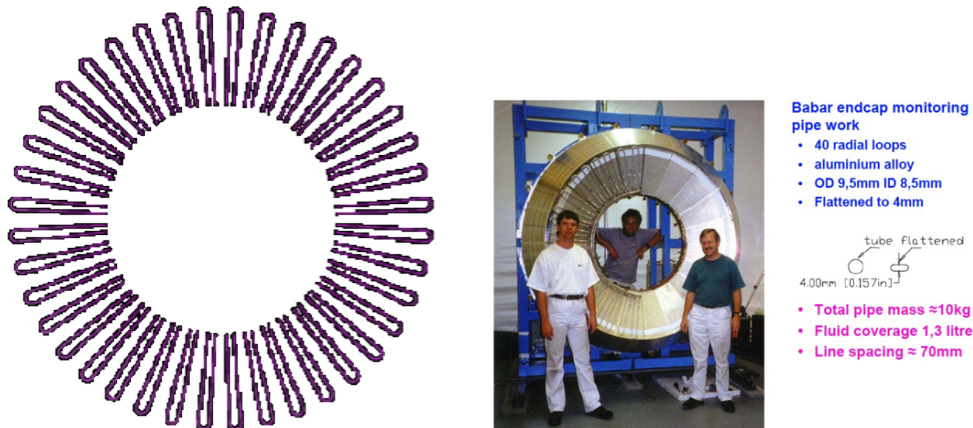


Figure 9.7: calibration circuit at the front of BaBar calorimeter

to neglect the resulting light losses and maximize photo device interface (e.g. 0,3 - 0,7mm).

#### 9.3.5.5 Module design

About 110 x 110 x 230 mm<sup>3</sup>, a very light container of 220g, supporting a mass of 25kg of crystals

Physical constraints Modules are displayed in 4 concentric rings containing growing numbers of 5x5 modules. Radial and tangential symmetries combine to produce a limited number of different crystal sizes, a simple assembly scheme, meanwhile satisfying the physics requisites (shower containment, light collection uniformity). Crystal subunits are grouped by 5 in  $\phi$  and 5 in  $z$  to form modules. There are 4 module types and 5 different crystals in  $\phi$  for each module type for a total of 20 crystal types. To achieve the required energy resolution, crystal-to-crystal separation must be less than or equal to half a millimeter. The design guarantees a maximum distance between crystal faces of 0.4 mm within a module and of 0.6 mm across two modules, either in  $\phi$  or in  $z$  for crystal nominal dimensions. For crystals with minimum tolerances these values are reduced by 0.1 mm. Inside a module, this distance results from the following contributions: the crystal processing tolerance, from 0 to 0.1 mm. a guaranteed air gap between the crystal nominal (maximal) shape and the alveolar container of 0.1 mm to

cope with the maximal alveolar unit elastic deformation in the worst case (crystals horizontal) and handling, transport or installation acceleration. Crystals do not take part in the structural resistance of the alveoli. the alveolar unit nominal wall thickness of 0.2 mm (including its manufacturing tolerance of 20  $\mu$ m). Between two modules, this distance results from the following contributions: the crystal processing tolerance from 0 to 0.1 mm, the 0.1 mm air gap inside the alveolar unit, the two facing walls of 0.1 mm each, an additional contribution of 0.35 mm due to the module copper shielding the 0.1mm gap between the two modules Space is left between modules to make assembly possible (module dimensional tolerances) for module-to-module mechanical connection insertion of prepreg fillers

The successful prototype of 5 x 5 size is considered an economic optimum (moulding cycle, handling, assembly, etc.) for the production aspects. The 5x5 modularity is also convenient for general architecture and integration front-end electronics modularity and connection and electromagnetic shielding. A 5x5 data matrices are also used in event reconstruction A small chamfer on the crystal edges is required because of the fragility of crystals and allows a small inner radius on the cell inside. This chamfer is also very useful for the polishing process.

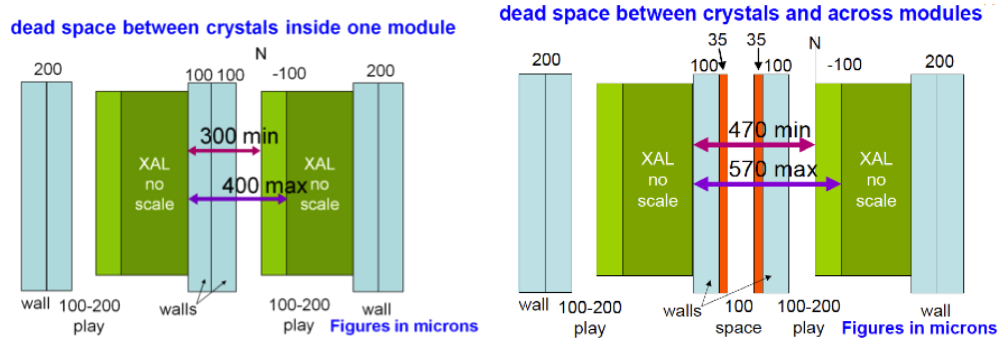


Figure 9.8: crack (crystal to crystal, left picture) and gap (module to module, right picture)

At the front of the crystal the cell is closed by an insert. The inserts are made of a CFRP with short C fibres in an epoxy matrix. This material is easy to machine and a good match for the insert complex shape. Although more expensive, carbon is preferred to glass as making less material in front of the crystal. It also ensures the electrical continuity with the Cu foil of the module electromagnetic shielding. The insert has a central hole used during alveola production. Few of these holes are used for the final module positioning in the Shell-Module and for the mechanical interface through composite setpins.

At the opposite side metallic clamps tightened on cell walls keep crystals in position

**Grounding and shielding** An aluminium foil inside the cell acts as a reflector for the crystal and provides electromagnetic shielding. The aluminium surface can be optically improved by a special metallic or transparent coating to enhance its reflectivity. Alveolar design must allow electrical contact between all conductive materials the Al reflecting foils of every cell in one alveolar should be electrically connected. Connection are in the cell rear empty space, through holes designed for crystal fixation.

Cell grounding just requires to put all cell Al reflectors in contact. Cell shielding needs additional metal thickness. Alveolar shielding is achieved by an ultimate Cu wrap of 50µm around sides on the external of the module. The Cu foil does not need additional adhesive film thickness as it is cured with the wall prepreg.

Price to pay is 100µm more dead space at every module to module transition. A similar foil is merged into the Support Shell bottom plate The bonded Cu foil, covering the four sides of the alveolar module, is connected to the cell ground.

?

**module supporting principles** Alveolar module are assembled into the Shell-Support-Structure (horse collar and wedge) Alveolar front ends are driven into position by 5 tubular CFRP setpins and the front of the module is glued to the structure front plate.

Alveolar back end sides are glued together via composite in ?. Connection between modules at the back reduces the bending moment of the alveola. Narrow glue strips are used because gluing of complete adjacent module walls is technically impossible. To achieve autoclave gluing of all modules in one operation the resin used for module front and sides has a lower curing temperature than that of the shell and modules. Alveolar unit moulding technique, precision, wall composition, radii and chamfers The alveolar container of a module is moulded in a precision CNC machined aluminium mould (tolerance of 0.02 mm) consisting of a box and a cover, and 25 mandrels with shapes similar to those of crystals.

The wall layers described next are wrapped around the mandrels. The mandrels are positioned with accurate setpins in precision holes of the mould box. A 50 micron Cu layer is wrapped all around the module before closing the mould. Closing the mould cover presses the



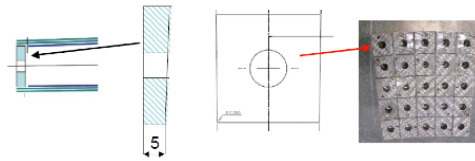


Figure 9.9: CFRP inserts at the front of the alveolar cells

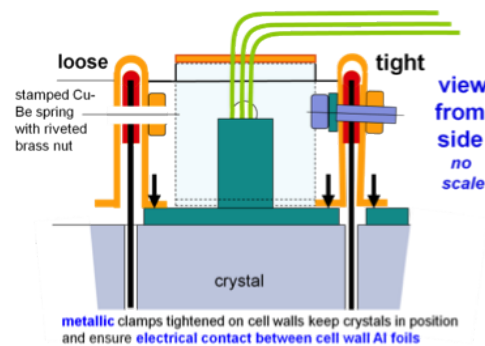


Figure 9.10: metallic clamps hold crystals in position

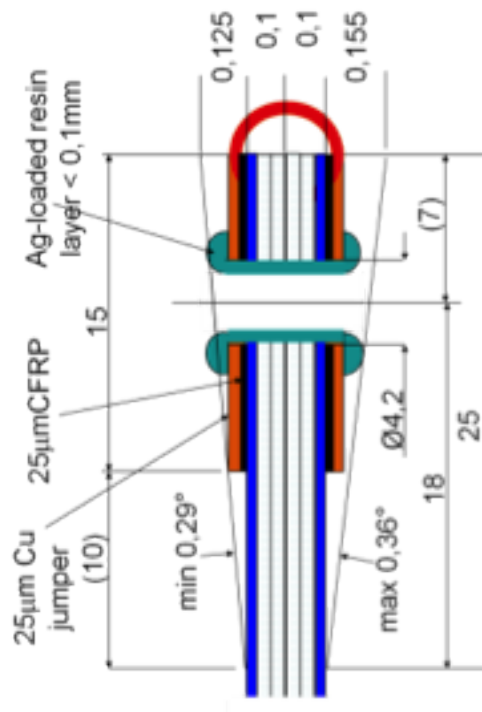


Figure 9.11: detail of the cell back open side

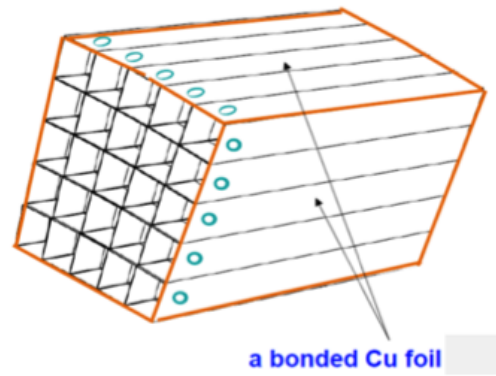


Figure 9.12: Cu foil around the module

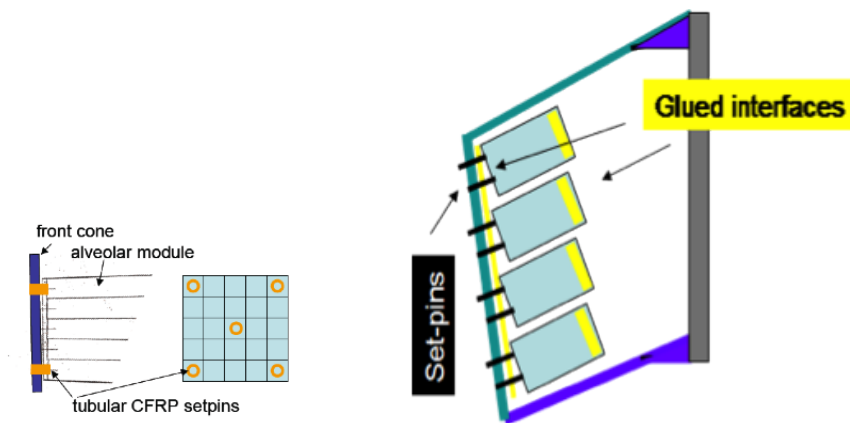


Figure 9.13: alveola supports

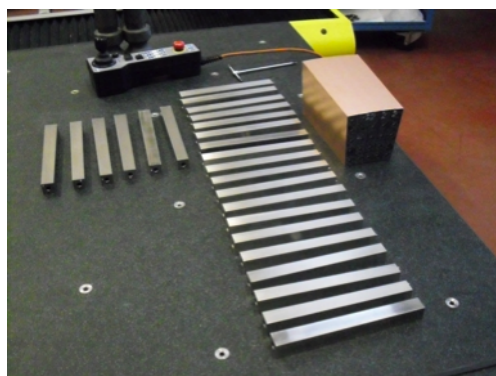


Figure 9.14: alveolar module mandrels

layers together and keeps the mandrels position with high accuracy. The moulding method requires a very uniform distance between the mandrels and the mould cavity in order to balance the very high pressures exerted when closing the mould and curing the resin. This is achieved by giving the mandrel the crystal theoretical shape increased by 0.1 mm (clearance between crystal and alveolar cavity).

The assembly is taken to the autoclave to cure the resin. This curing is performed at 120 for 90 minutes, plus the time to reach the curing temperature and to cool down. A finishing of the ends of the module is performed after the extraction of the mandrels.

The wall of the alveola is as follow. The first layer consists of an aluminium foil of a thickness of 25 microns and has a triple function. It rigidifies the alveolar unit, acts as a reflector for the crystal and provides electromagnetic shielding. The aluminium surface can be optically improved by a special metallic or transparent coating to enhance its reflectivity. The second layer consists of a glass fibre epoxy resin prepreg of a thickness of 75 microns. The 75 microns is obtained by the wrapping of two layers, 35 microns, of FGRP (Fiber Glass Reinforced Plastic). This material has been selected for its ability to produce very thin walls with a very small radius of curvature. Given wall thickness and radius limit, the combination of fibre material and diameter is such to avoid edge breaking at moulding and ensure cell structure integrity. Glass fibre is also very economical and easy to process. The 0.02 mm accuracy of the moulding is consistent with the alveolar unit tolerances. The total thickness of glass fibre wrapped around a mandrel is nominally 100 microns. The resulting surface density of material between two crystals is 200 g/m<sup>2</sup>. No other material can produce walls thin enough to maintain the gap between crystals to 0.4 mm. Compared to carbonfibre, glass fibre has a relatively low elasticity modulus and can be formed with a sharper bending radius. Mandrels producing the inner shape are chamfered at 0.3 mm ? 45.

**Module Prototypes** To validate the submodule design, two prototypes of the alveola module have been constructed.

**Proto1** A first prototype was produced to validate the cell structure concept and the production economy. It was then used with its 25 crystals in a beam of particles for physics validation. The Proto1 validate the whole production process and a 3D dimensional inspection performed on the internal and external walls gave evidence of the achievable dimensional tolerances. Wall thickness was measured at the cell open edge over 20mm depth on both sides of punched holes and produced the following values : a) for internal walls nominal 0,200mm 0,15 to 0,22 b) for external walls nominal 0,135mm 0,13 to 0,17

The information gathered have been used to define the production protocol.

**Proto2** A second prototype was produced in September 2011 to confirm process repeatability and to evaluate the global mechanical properties of the structure. The alveolar module is identical to that used for the physics beam test in October 2010, Proto1. The test campaign had the aim to evaluate the structure overall mechanical properties. Global deformations of the alveolar array are significant, and a loading test is essential for checking the absence of interference with the shell inside (inner and outer cone) and the absence of crystal stressing (cell bending ; play) in a first approximation. The cell were loaded with dummy crystals that simulate the mass and different gravity vectors have been investigated. The mechanical tests performed on the modular structure provided basic input data to a Finite Element Analysis of the complete support structure.

#### 9.3.5.6 Alveolar module structure finite element analysis

A detailed Finite Element Analysis was performed on the alveolar structure using material properties from data-sheet. The analysis predictions have been compared with the outcome of the load test on Proto2 and the model tuned to best fit the real behaviour. This detailed model has been used as reference to validate the Global Finite element model of the whole EMC.



Figure 9.15: alveolar module production process

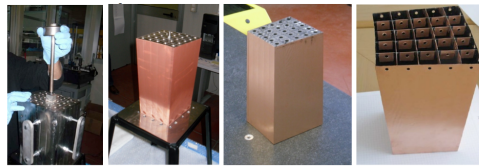
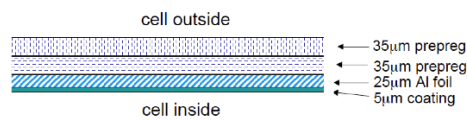
Figure 9.16:  
alveolar module production process

Figure 9.17: cell wall

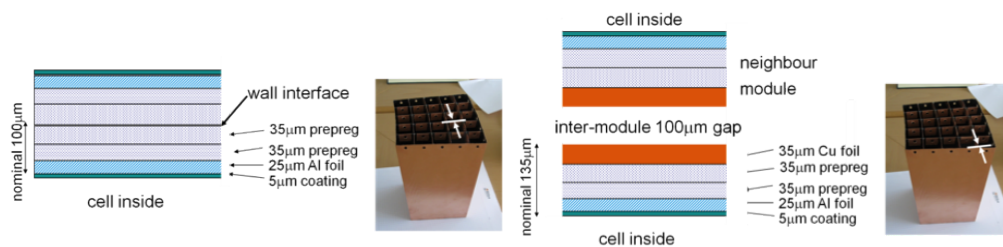


Figure 9.18: alveolar module walls internal and external

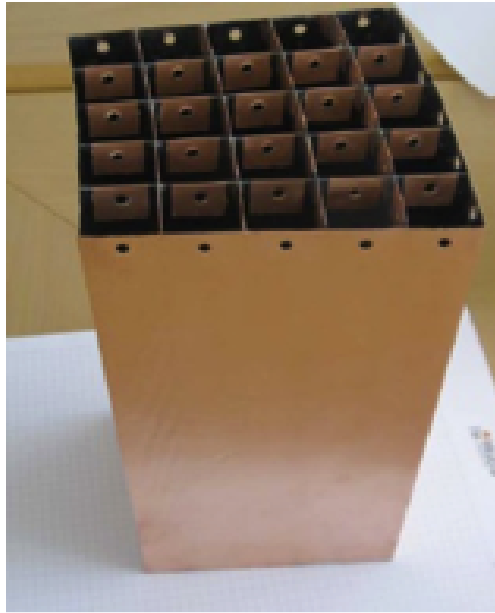


Figure 9.19: alveolar module prototype

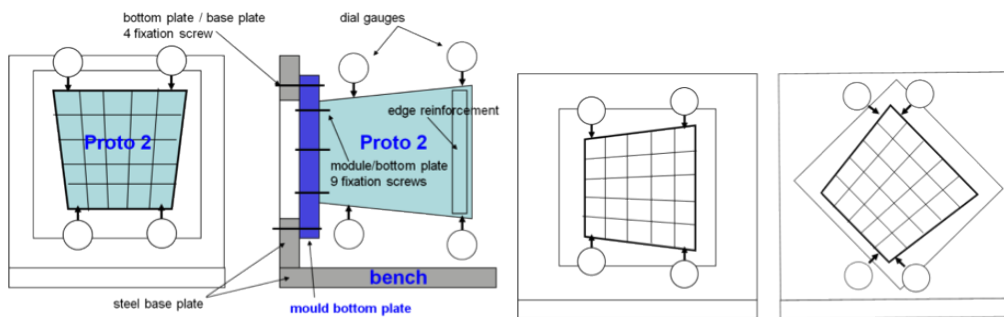


Figure 9.20: alveolar module test setup

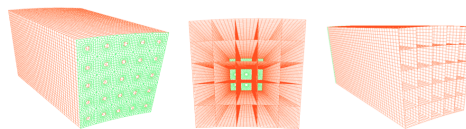


Figure 9.21: alveolar module finite element model

### 9.3.5.7 Support shell structure design

The shell consists of the outer cone and front cone as one single solid body in CFRP. The inner cone, where material budget does not pose too stringent limits is a metallic shell. Back plate is the same as BaBar. The volume is defined by the line AB, AD, CD while A'B' and A'D' are construction lines resulting from technical choice.

The outer cone end is reinforced by a metallic ring for easy connection with the back plate. The back plate provides the EMC interface with the SuperB bearing points (position reference and transmission of loads). The alveolar array is cantilevered from the shell front cone.

This configuration reduces provides a logical construction and assembly sequence, in particular an easier and almost reversible access to the most delicate part of the detector, its crystals and photodiodes. There is no connection between the alveolar array and the inner and outer cone inner faces. A 1mm gap is introduced for the free elastic deformations of the alveolar array and of the shell. The front cone is connected to the inner cone by gluing secured by screws.

Support Shell unit production and materials  
The outer cone is a massive CFRP (6 to 10mm) while the front cone is either a massive CFRP or a sandwich plate 20mm thick. For the production the mould is at the inner face of the outer-front cone in order to have high dimensional accuracy at the interface with the crystals modules, while a vacuum bag is at the opposite side; the parietal aluminum wedge is embedded in the structure. The inner cone is a precise CNC machined massive Al 7075 piece with a thickness of 20mm.

### 9.3.5.8 Global structure finite element analysis

To the front conical plate are connected 180 alveolar modules (of 5 x 5 cells) of four different types, displayed in four concentric rings. Because of the circular configuration each module is in a different loading case. The resulting FE model of the complete distribution of alveolar modules supported by the shell structure would

result in a large size, . An alternative parallel solution was followed to reduce the alveolar module to its main useful parameters (super-elements) that do not contain all the geometrical detail but that closely characterize the mechanical behaviour of the alveola. The inut mechanical properties used for the superelements come from the mechanical tests performed on the Proto2.

### 9.3.6 Performance in simulations[SG]

#### 9.3.6.1 Resolution studies

Can include comparison with *BABAR* forward calorimeter

#### 9.3.6.2 Background studies

### 9.3.7 Tests on Beam[CC]

#### 9.3.7.1 Description of apparatus

Two tests beam have been performed with a prototype LYSO matrix, one at CERN in October 2010 and one at the Beam Test Facility (BTF) in Frascati in May 2011. The prototype matrix is composed by 25 LYSO crystals of pyramidal shape with dimensions  $2.3\text{cm} \times 2.3\text{cm} \times 22\text{cm}$  inserted in a support structure assembled by the RIBA company (Faenza, Italy). Each crystal presents a black band of 15mm at the end of its smallest face to improve the uniformity light output, and also the area of the face not covered by the APD (or PiN) is painted with a reflective white painting. The mechanics is composed of glass fiber, covered with copper foils  $35\mu\text{m}$  thick. Between one cell and the other there is a nominal thickness of  $200\mu\text{m}$ , while the external side has a thickness of  $135\mu\text{m}$ . Fig.9.3.7.1 shows a picture of the Test Beam structure with inserted one raw of crystals. Each crystal is readout with an Avalanche Photodiode (APD) for 20 crystals and with a PiN Diode for the remaining five at the Beam Test at CERN, while at the BTF all crystals are equipped with APD's. The electronic front end board (VFE) used to readout the photodetectors contains a Charge Shaper Preamplifier (CSP), then the signal is sent to a Shaper Range Board which complete the attenuation, already applied in the VFE board,

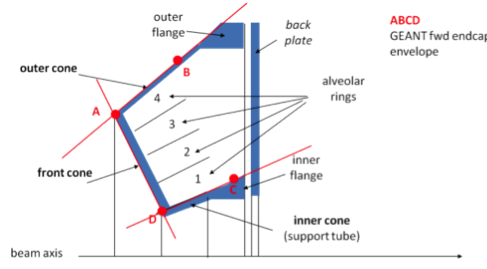


Figure 9.22:

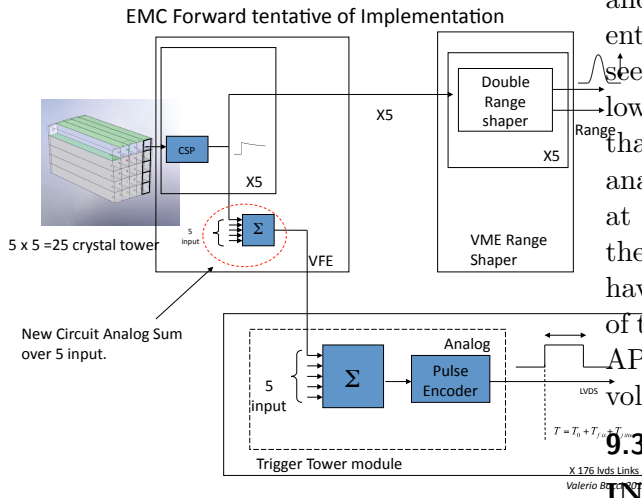


Figure 9.27: Schematic view of the electronic chain for the forward EMC.

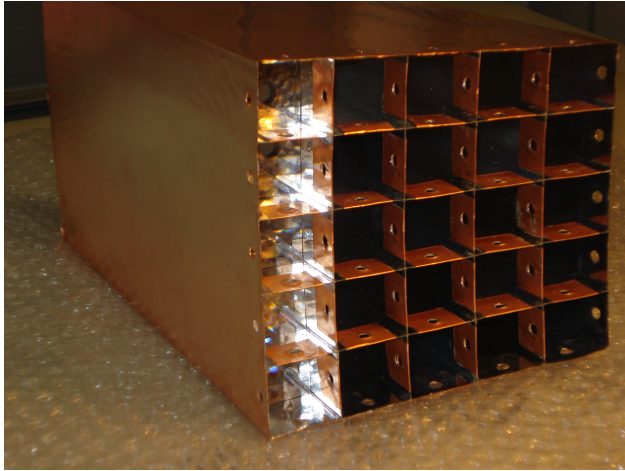


Figure 9.26: Picture of the Test Beam mechanical structure with one row of LYSO crystals.

and then divide them according to the different energy range. Two different ranges are foreseen in the treatment of the signals, for energies lower than 200 MeV and for energies greater than 200 MeV. The processed signals and the analogue output are acquired by four ADC Caen at 12 bit. Fig. 9.27 shows a schematic view of the readout chain. Two different configurations have been used at CERN for the power supply of the APD's, one called High Gain with voltage APD at 380V and one called Low Gain with a voltage of 308V applied.

### 9.3.7.2 Electronics noise measurements

#### INTRODUCED BY RF FROM THE TB NOTE

The noise of each crystal  $i$  is analyzed in the Fourier space, by estimating its power spectrum from waveforms acquired with a random trigger:

$$PS_i(\omega_k) = \langle n_i(\omega_k) n_i^*(\omega_k) \rangle \quad (9.1)$$

where  $\omega_k$  is the  $k$ -th component of the discrete Fourier transform (DFT) of a noise waveform, and  $\langle \rangle$  denotes the average taken over a large number of waveforms. We recall that the quantity that contributes to the energy resolution is the noise fluctuation in the time domain ( $\sigma_i^{\text{noise}}$ ), which can be expressed in terms of Eq. 9.1 as:

$$\sigma_i^{\text{noise}} = \sqrt{\sum_k PS_i(\omega_k)}. \quad (9.2)$$

Estimated power spectra of four representative crystals are shown in Fig. 9.28, where it

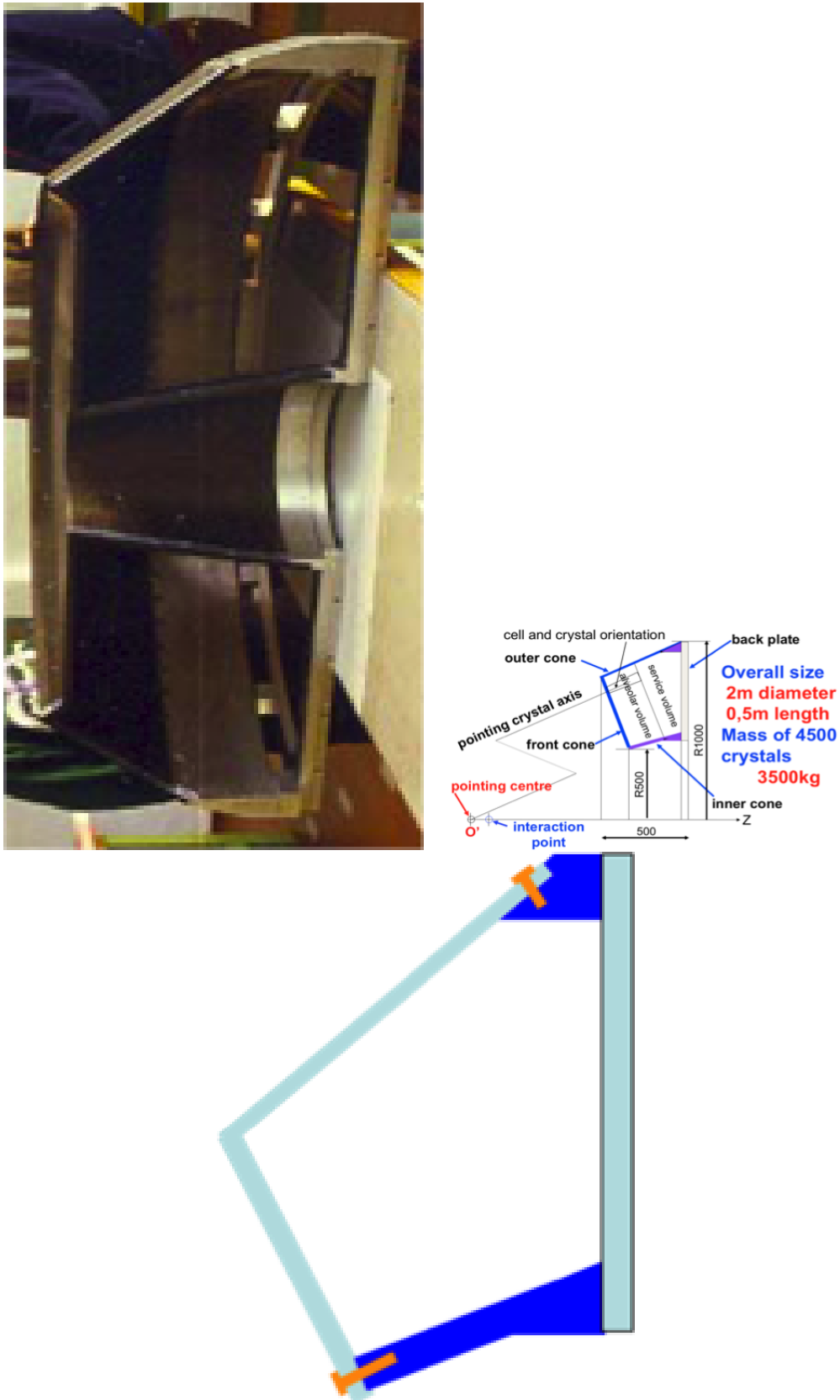


Figure 9.23:



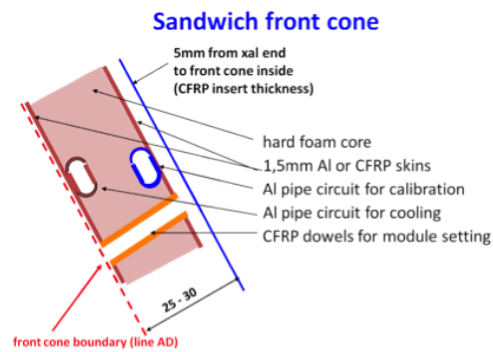


Figure 9.24:

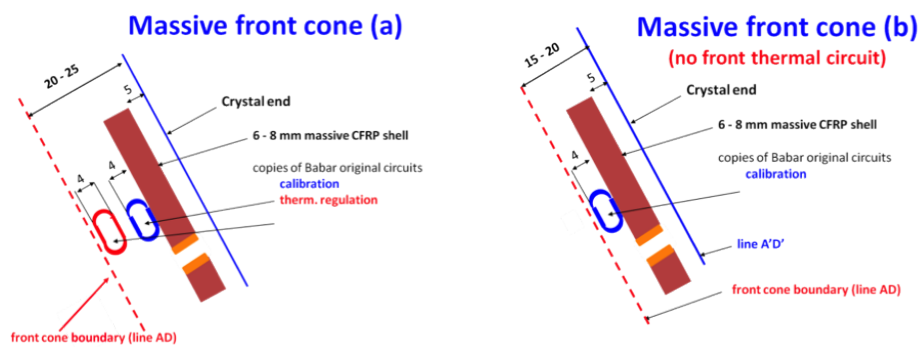


Figure 9.25:

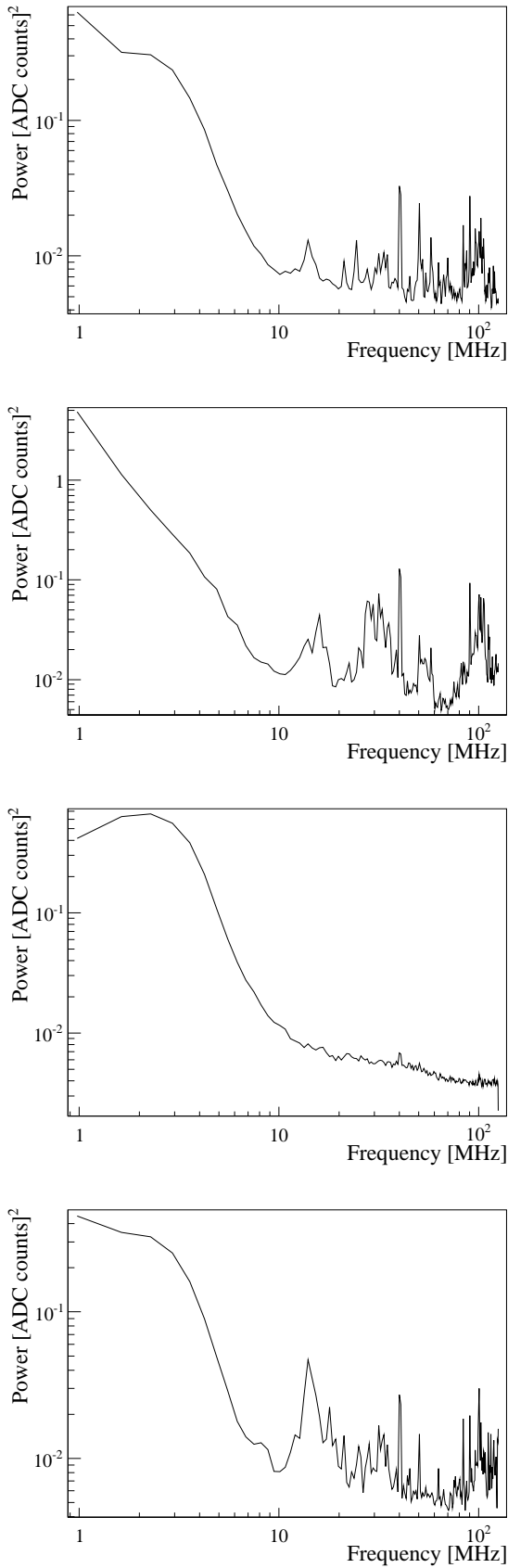


Figure 9.28: Noise power spectrum measured on crystals 10 (top left), 18 (top right), 12 (bottom left) and 2 (bottom right).

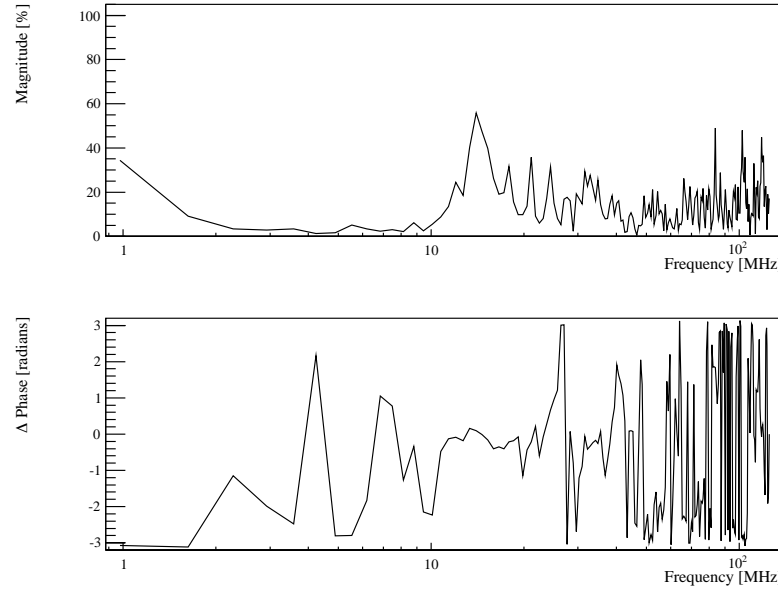


Figure 9.29: Correlation between crystals 2 and 10 as a function of the frequency. The phase takes random values when the magnitude is zero, when this happens its value should not be considered.

can be seen that the dominant source of noise is in the range 0-8 MHz, which corresponds to the frequency bandwidth of the shaper. Sources of noise occurring after the shaper give a negligible contribution, while those occurring before are filtered according to the shaper transfer function and dominate. The noise fluctuation  $\sigma_{\text{noise}}$  was found to be, averaged over all channels, 2.1 ADC counts, with a dispersion max-min equal to 0.3 ADC counts. Crystal 18 was the only outlier with  $\sigma_{\text{noise}} = 3.3$  ADC counts.

We investigated the presence of a possible correlation between the noise observed on different crystals. The correlation can be in principle present, because the APDs in the matrix are biased by a unique power supply, and each Front End board serves 5 crystals. If the noise is found to be correlated, it would point to a common source of noise that hopefully can be identified and removed.

The covariance between crystals  $i$  and  $j$  has been estimated as

$$\text{COV}_{ij}(\omega_k) = \langle n_i(\omega_k) n_j^*(\omega_k) \rangle \quad (9.3)$$

where the definitions are the same as in Eq. 9.1. The magnitude of an element of these matrices is the covariance between two crystals as usually intended in the real domain, while the phase is the relative time delay between them. As a consequence the correlation is also a complex quantity, which is defined as:

$$\rho_{ij}(\omega_k) = \frac{\text{COV}_{ij}(\omega_k)}{\sqrt{\text{PS}_i(\omega_k) \text{PS}_j(\omega_k)}}. \quad (9.4)$$

The two crystals with the highest correlation below 8 MHz were number 2 and 10, and the corresponding plot is shown in Fig. 9.29. It can be seen that the correlation is, on average, very small in the region of interest. Fig. 9.30 summarized the correlation matrix averaged in the ranges 0-8 MHz, 8-40 MHz and 40-125 MHz. The plots indicate that the noise correlation is negligible, and that each crystal has an independent noise source.

### 9.3.7.3 Description of beam

The Beam Test at CERN has been performed at the T10 beam line in the East Area. The

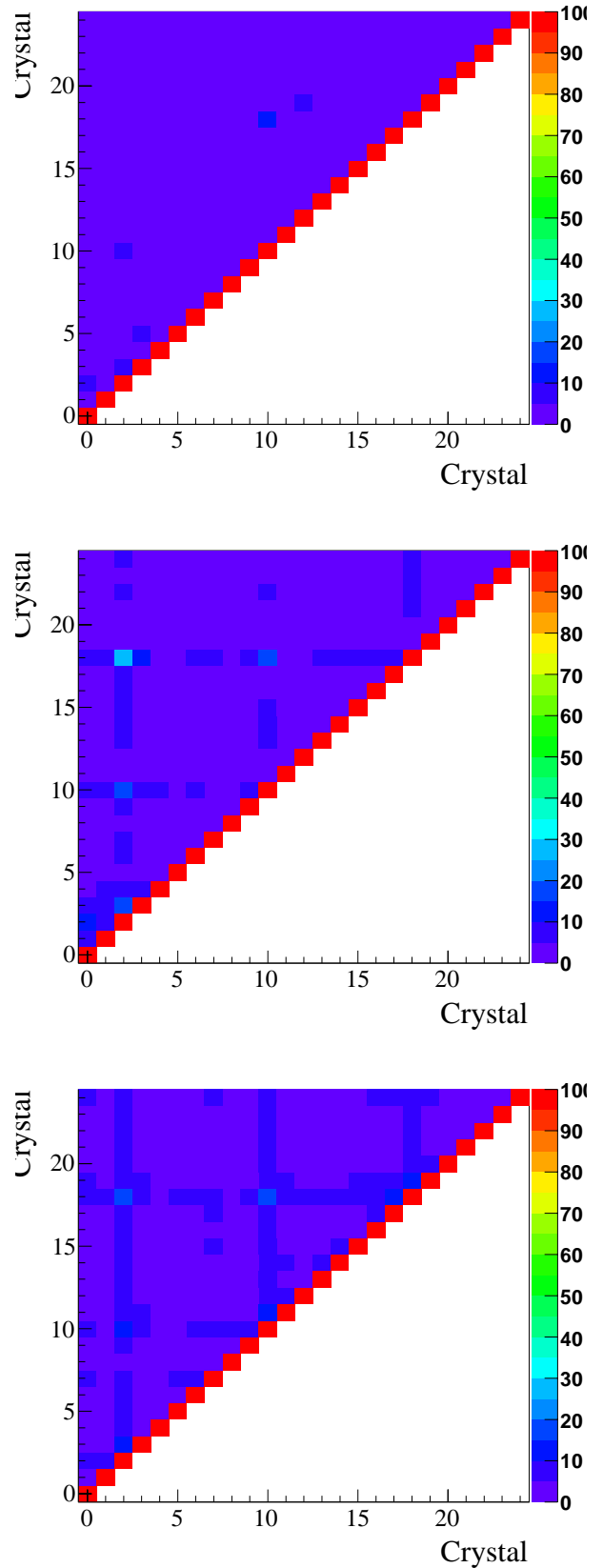


Figure 9.30: Noise average correlation in different frequency bandwidths, 0-8 MHz (top left), 8-40 MHz and 40-125 MHz.

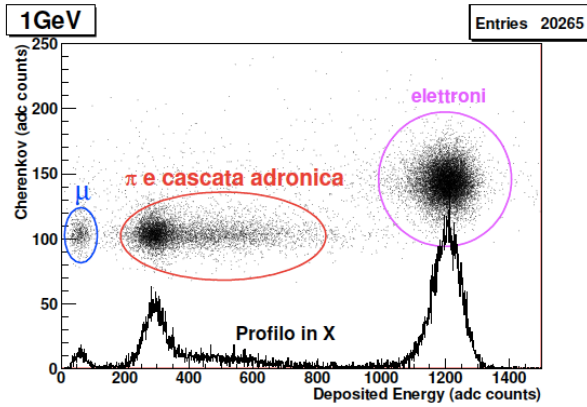


Figure 9.32: Distribution of the signal measured in the Cherenkov detector as function of the total energy deposited in the calorimeter, at 1 GeV.

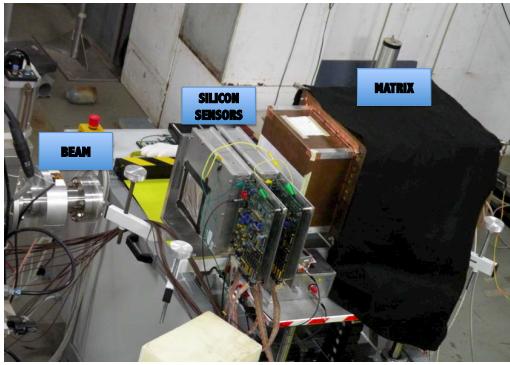


Figure 9.33: Schematic view of the test beam setup used at the BTF in Frascati.



Figure 9.31: Schematic view of the test beam setup used at CERN.

beam is mainly composed of electrons, muons and pions created by the scattering of protons into aluminum and tungsten target. The composition of the beam is highly dependent on the energy and for electrons goes from 60% at 1 GeV to 1% at 6 GeV. The maximum energy reachable at this beam line is 7 GeV with a momentum spread  $\Delta p/p \simeq 1\%$ . The distance between the end of the beam line and the matrix is about 15 m. The event rate is of the order of 1 Hz.

Fig.9.31 shows the experimental setup used at CERN, it is composed of a Cherenkov detector already present in the CERN beam line, two scintillators (finger counters)  $2 \times 2 \text{ cm}^2$ , the box containing the matrix and the VFE boards. The Cherenkov detector plus the two scintillators of the fingers act as trigger. The Cherenkov detector allows the separation between electrons and pions as shown in Fig.9.32. The same detector has also been used to select Minimum Ionising Particles (MIP) used for the calibration.

The Beam Test Facility in Frascati is part of the  $\Phi$ Factory, DaΦne. It is composed of a linear accelerator LINAC, one spectrometer and two circular accelerator of electrons and positrons at 510 MeV. The LINAC is the same which supplies the test beam line at the BTF. The pulsed beam of the LINAC circulate electrons up to 800 MeV at a maximum current of 550 mA/pulsation and positrons at a maximum energy of 550 MeV with a current of 100 mA/pulsation. The typical duration of a pulsation is 10 ns, with a frequency of 50 Hz. A bending magnet select electrons of a given momentum, a line of about 12m contains quadrupoles for the uniformation of the beam and a system of slits allow to change the flux of arriving particles. The beam energy spread is 1% at 500 MeV. The setup for the beam test of the matrix at the BTF is shown in Fig.9.33. The setup shows the end of the electron beam line, four planes of silicon strip detector (two measurements in x and two measurements in y) and the box containing the matrix with the crystals and the VFE boards. As mentioned before, at the BTF all the crystals are equipped with APD's,

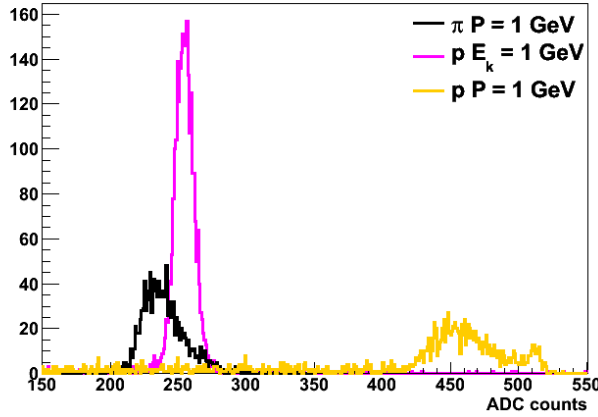


Figure 9.34: MC simulation of the energy released by MIPs in the high gain configuration.

and it should be mentioned that the gain of the VFE has changed with respect to CERN from 0.5 to 1, while an amplification factor has been introduced. To control the position of the beam with respect to the matrix a detector of  $16 \times 16$  scintillating fibers of 3mm each has been used. The trigger is performed by the LINAC radiofrequency (25 Hz), and does not make any use of scintillators.

#### 9.3.7.4 Description of data

#### 9.3.7.5 Calibration

**INTRODUCED BY RF FROM THE TB NOTE Modified by CC** Charged hadrons release in a significant fraction of cases a known amount of energy in a single crystal and this makes this sample particularly suited to intercalibrate the crystals and to study corrections to the energy measurement. The criteria described in Sec. ?? select events where the charged hadrons release their energy exclusively by ionization in a single crystal. Such events are therefore labelled as minimum ionizing particles (MIP). The raw energy of a MIP is the energy measured in the only crystal with significant energy. MIP are selected using the information of the Cherenkov detector and using the energy deposited in each crystal which is described by a Landau distribution. For each

of the 25 crystals a fit to this distribution has been performed measuring the most probable value (MPV) and a  $5 \times 5$  matrix has been obtained. Taking the central crystal (number 12) as the reference and dividing all the matrix by the MPV of the crystal 12 the intercalibration matrix is obtained. The energy deposited in each crystal is then corrected by this correction factor to have a calibrated value of the energy. The calibration is evaluated for each configuration "Low" and "High" gain. When performing studies with this sample we will call "energy" the raw energy multiplied by a factor that matches the mean value in data with the expectation from simulation.

At the BTF, due to the fact that only electrons are present in the beam the intercalibration has started using the information from cosmic muons.

#### 9.3.7.6 Data-MC comparison

The detailed simulation described in Sec. ?? has been used to estimate the expected MIP energy spectrum. Since the beam could potentially contain both protons and pions with the same momentum, both were considered. Their energy spectrum, shown in Fig. 9.34 in the case of  $p = 1\text{ GeV}$ , reveals that pions and protons are significantly different. The relative RMS (mean) of the distributions for pions and protons are 6.3% (240 MeV) and 5.4% (460 MeV) respectively. The spread in the measured energy is dominated by fluctuations in the energy loss and therefore this sample cannot be used for resolution studies.

The distribution of the energy released in the MIPs sample after selection in the high gain configuration is compared with MC expectations in Fig. 9.35. There is good agreement between the distributions under the hypothesis that only pions are present in the sample.

The comparison between the energy measured in the case of high and low gain after normalization to the same energy scale (Fig. 9.36) and after releasing the constraint on the pad behind the crystal matrix shows that the spread is comparable, thus confirming that it is domi-

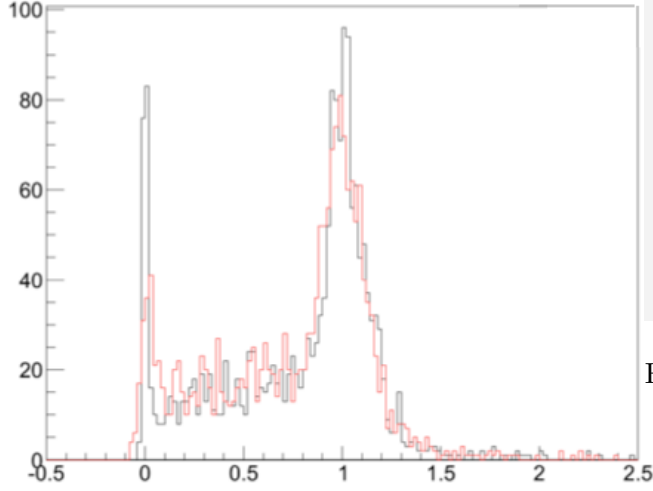


Figure 9.36: Comparison between the distributions of the measured energy separately in the low gain (red) and high gain (black) samples. The energy scales are normalized to enforce the peak at the value of 1.

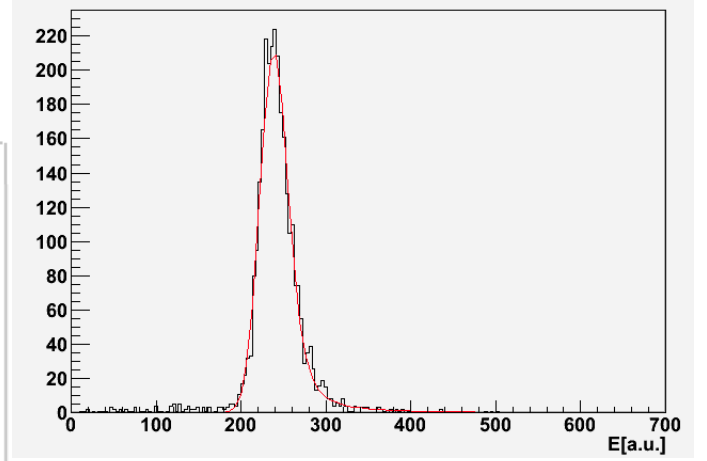


Figure 9.37: Energy distribution of a MIP with the fit to a Landau convoluted with a gaussian superimposed.

Table 9.3: Intercalibration constants estimated with MIPS. The matrix represents the crystal matrix and the numbers in square brackets is the corresponding crystal id.

[0]	$2.106 \pm 0.024$	[1]	$2.058 \pm 0.017$	[2]	$2.972 \pm 0.017$	[3]	
[5]	$1.263 \pm 0.008$	[6]	$1.085 \pm 0.004$	[7]	$0.5379 \pm 0.003$	[8]	
[10]	$1.757 \pm 0.012$	[11]	$0.886 \pm 0.004$	[12]	$1.000 \pm 0.003$	[13]	
[15]	$1.265 \pm 0.014$	[16]	$1.148 \pm 0.008$	[17]	$1.220 \pm 0.010$	[18]	
[20]	$0.629 \pm 0.005$	[21]	$1.134 \pm 0.009$	[22]	$1.133 \pm 0.011$	[23]	

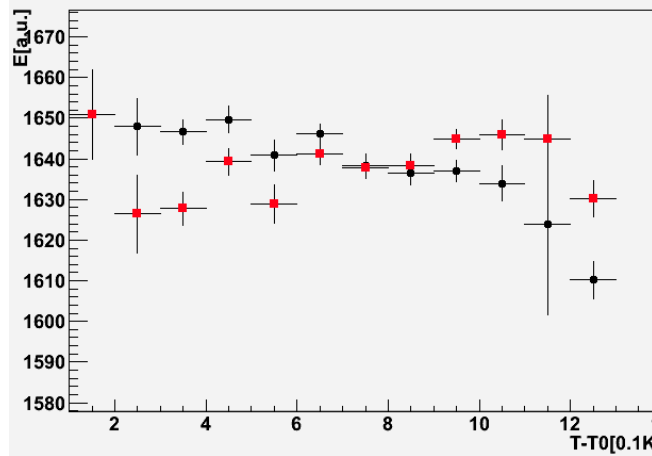


Figure 9.38: Dependence of the measured energy on the temperature before (black dots) and after (red squares) correction.

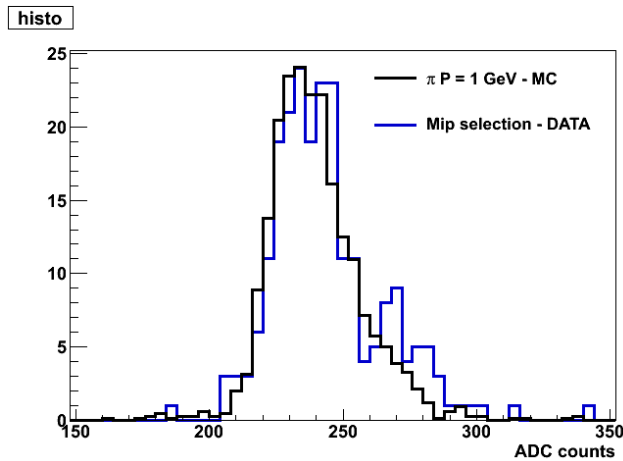


Figure 9.35: Comparison between data and MC under the pion hypothesis of the energy deposited in the MIPs sample.

nated by fluctuations in the energy release. It also shows that the pedestal widths scale with the gain and that therefore the source of the noise is upstream of the amplifier. **REVIEW ARGUMENT**

Since MIPS release their energy in just one crystal they are an ideal sample to intercalibrate crystals. To this aim several runs were

taken moving the crystal matrix in such a way that each crystal in turn has been shot by the beam in the middle. The mean value of the deposited energies should be the same modulus the fact that each crystal presented a different angle with respect to the beam line. Corrections for this effect were calculated with MC simulation and revealed to be negligible. The distributions of the deposited energies after temperature correction were fitted with the convolution of a landau distribution and a gaussian resolution (see Fig. 9.37). The intercalibration constant of a crystal were estimated by dividing the mean value of the deposit in the central crystal (#12) by the corresponding mean value in the crystal itself. The measured constants are summarized in Tab. 9.3.

### 9.3.7.7 Temperature corrections

A temperature dependence of several percent per degree is expected both in the light yield of the LYSO crystals and in the gain of the APDs. The position of the MIP peak as a function of the temperature measured by the sensors (Fig. 9.38) has been used to extract the temperature correction:

$$E_{corr} = E_{raw} / (1 - p_0 * (T - T_0)) \quad (9.5)$$

where  $p_0 = 2.8 \pm 0.2 \times 10^{-3}$  and  $T_0 = 34K$ . The same figure shows also the effect of the correction.

## WHERE ARE THE SENSORS DESCRIBED?

### 9.3.7.8 Algorithms and results

## 9.3.8 Alternatives

### 9.3.8.1 Alternative 1

Description

- Performance, tests
- Mechanical changes
- Electronics changes

### 9.3.8.2 Comparison with baseline

Includes a brief discussion of other, discarded, options

I got here!



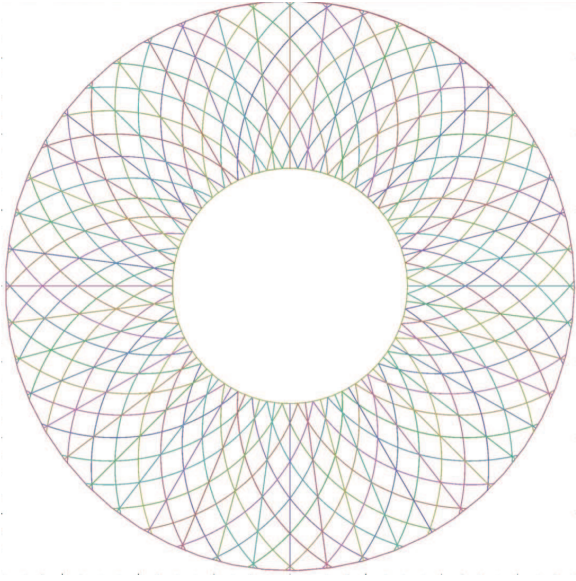


Figure 9.39: The backward EMC, showing the scintillator strip geometry for pattern recognition.

## 9.4 Backward Calorimeter

The backward electromagnetic calorimeter for SuperB is a new device with the principal intent of improving hermeticity of the detector at modest cost. Excellent energy resolution is not a requirement, since there is significant material from the drift chamber in front of it. Thus a high quality crystal calorimeter is not planned for the backward region. The proposed device is based on a multi-layer lead-scintillator sampling calorimeter with longitudinal segmentation providing capability for  $\pi/e$  separation. The design is derived from the analog hadron calorimeter for the ILC.

The backward calorimeter is located behind the drift chamber starting at  $z = -1320$  mm (see Figure ??) allowing room for the drift chamber front end electronics. The inner radius is 310 mm, the outer radius is 750 mm and its total thickness is less than 180 mm covering  $12X_0$ . It is constructed from a sandwich of 2.8 mm Pb plates alternating with 3 mm plastic scintillator strips (*e.g.*, BC-404 or BC-408). The

scintillation light of each strip is collected by a wavelength-shifting fiber (WLS) coupled to a photodetector located at the outer radius. The scintillator strips come in three different geometries, right-handed logarithmic spirals, left-handed logarithmic spirals and radial wedges. This pattern alternates eight times. Each layer contains 48 strips producing a total of 1152 readout channels. The strip geometry is illustrated in Fig. 9.54

The WLS fibers, Y11 fibers from Kuraray, are embedded in grooves milled into the center of the scintillator strips. Each fiber is read out at the outer radius with a  $1 \times 1$  mm<sup>2</sup> multi-pixel photon counter (SiPM/MPPC) [6]. A mirror is glued to each fiber at the inner radius to maximize light collection. The SPIROC (SiPM Integrated Read-Out Chip) integrated circuit (IC) [7] developed for the ILC is used to amplify and digitize the SiPM/MPPC signals, providing both TDC (100 ps) and ADC (12 bit) capability. Each ASIC contains 36 channels. Since these ASICs were developed for SiPM readout, where the intrinsic gain is much higher, an additional preamplifier is coupled to the SiPM/MPPCs. This has the advantage to place the SPIROC ASICs at a convenient place in the detector without introducing additional noise.

### 9.4.1 Improvements on physics results

The study of the leptonic decay  $B \rightarrow \tau\nu$  is of particular interest as a test of the Standard Model (SM) and a probe for New Physics. The presence of a charged Higgs boson (in *e.g.*, a Two Higgs Doublet Model) as a decay mediator could significantly enhance the branching ratio above the SM value. A detailed analysis of this channel is therefore quite important in searches for physics beyond the SM.

The  $B \rightarrow \tau\nu$  decay is challenging to identify, as the final state contains many neutrinos and can only be partially reconstructed. Signal events are selected using a recoil analysis, where the signal  $B$ -meson is identified as the recoiling system against the other (tag)  $B$  meson. The tag  $B$ -meson is either fully reconstructed via its hadronic decays [?], or partially reconstructed



from its semileptonic  $B \rightarrow D^0 \mu \nu_\mu$ ,  $D^0 \rightarrow K \pi$  decays. The rest of the event is assigned to the  $B \rightarrow \tau \nu$  candidate, and must be compatible with one of the following decay modes of the tau lepton:  $\mu \nu_\mu \nu_\tau$ ,  $e \nu_e \nu_\tau$ ,  $\pi \nu_\tau$ ,  $\pi \pi^0 \nu_\tau$ ,  $\pi \pi^0 \pi^0 \nu_\tau$ ,  $\pi \pi \pi \nu_\tau$ ,  $\pi \pi \pi \pi^0 \nu_\tau$ . These final states cover about 95% of the total  $\tau$  width, and have one (1-prong) or three (3-prong) charged particles, with the possible addition of a  $\pi^0$ . Since final states containing one or more  $\pi^0$  cover about 40% of the tau decay modes, an increase in the EMC coverage improves substantially the efficiency of tau identification.

A large background arises from  $B$ -meson decays with undetected or misidentified particles, such as  $B \rightarrow \pi^0 \ell \nu$  or  $B \rightarrow \eta \ell \nu$ . These backgrounds are further rejected using,  $E_{extra}$ , the total neutral energy in the detector of particles not associated with either  $B$ -meson. Signal events peak at low  $E_{extra}$ , while background events, which contain additional sources of neutral clusters, tend to be distributed at higher values. The discriminating power of this variables obviously increases with the calorimeter coverage. The signal and background levels are finally extracted by fitting the beam-energy substituted mass  $m_{ES} = \sqrt{s/4 - p_B^2}$  distribution of the tag  $B$ -mesons.

The performance of the backward EMC is assessed by comparing the signal-to-background ratio,  $S/B$ , and the statistical precision,  $S/\sqrt{S+B}$ , of the expected signal with and without the backward EMC. The addition of the backward EMC increases the signal-to-noise ratio by  $\sim 18\%$  ( $\sim ??\%$ ) and the statistical significance by  $\sim 4\%$  ( $\sim ??\%$ ) for hadronic (semileptonic)  $B$ -tagging. It is worth mentioning that the inclusive of the backward EMC not only improves the background rejection, but the  $B$ -tagging efficiency as well.

### 9.4.2 Requirements

The main goal of the backward endcap EMC is to record any charged or neutral particle. This information is important for analyses that study the recoil of a  $B$  meson fully reconstructed in hadronic or semileptonic to reduce backgrounds. Recording extra energy in the detector allows

for background rejection. Furthermore, the time-of-flight and energy loss via ionization capability is useful to perform particle identification.

#### 9.4.2.1 Energy and angular resolution

Since the backward EMC prototype is still in the construction phase, presently no results on energy resolution and angular resolution exist. However, electromagnetic sampling calorimeter prototypes with plastic scintillator strips and tiles have been tested in test beams within the CALICE collaboration [?]. The energy resolution for the stochastic term is  $15\% \sqrt{E}$  and for the constant term is around 1%. For the CALICE analog hadron calorimeter which has a non-optimized geometry for electromagnetic showers, the stochastic term was measured to be around  $20\%/\sqrt{E}$ . For low photon energies, an additional noise term of  $\sim 130 \text{ MeV}/E$  contributes. Thus, the backward endcap EMC is expected to have a similar performance with a stochastic term of  $15 - 20\%/\sqrt{E}$ .

The left-handed logarithmic spirals are defined by

$$x(t) = r \exp b \cdot t \cos t - r \quad (9.6)$$

$$y(t) = r \exp b \cdot t \sin t \quad (9.7)$$

$$(9.8)$$

For  $r = r_o/2 = 37.5 \text{ cm}$  and  $b = 0.2$  eight left-handed spiral strips overlap with eight right-handed spiral fibers defining a specific tile-shaped region. The radial strips overlap with five left-handed (right-handed) spiral strips. In the worst case the resolution is  $\sigma_r = \sigma_\phi \simeq 29 \text{ mm}$  in the outer region. This is improved to  $\sigma_r = \sigma_\phi \simeq 12 \text{ mm}$  in the inner region.

#### 9.4.2.2 Background rates

Present background simulations indicate that the worst n rate in layer zero of the backward IFR end cap is  $3.5 \text{ kHz/cm}^2$ . The radiation profile shown in Figure ?? indicates that the worst rates for all energies of  $3 \text{ kHz/cm}^2$  occur in the inner most region. In ten years of running this amounts to  $6.1 \times 10^9 \text{ n/mm}^2$  in the region near the inner radius. The background rates

drop by significantly towards outer radius. At the the location of the photodetector, the rate is reduced by more than a factor of 10. Further simulation studies are needed, since due to the high rate at the inner radius an occupation problem may be present. To deal with this issue one either subtracts a higher average background energy from each strip or divides the strips into two segments at the cost of doubling the number of photodetectors. The former solution will have an effect on the energy resolution since the background energy deposit has a wide distribution. The latter solution is preferable, but is about \$100k more expensive.

#### 9.4.2.3 Radiation hardness

Irradiation of Si detectors causes the dark current to increase linearly with flux  $\Phi$ :

$$\Delta I = \alpha \Phi V_{eff} G, \quad (9.9)$$

where  $\alpha = 6 \times 10^{-17} \text{ A/cmV}_{eff} \sim 0.004 \text{ mm}^3$ ,  $\Phi$  is the flux,  $V_{eff}$  is the bias voltage and  $G$  is the gain. Since the initial resolution of SiPMs of  $\sim 0.15pe$  is much better than that of other Si detectors, radiation effects start at lower fluxes. For example, at a flux  $\Phi = 10^{10}/\text{cm}^2$  the individual single pe signals are smeared out. The MIP peak is still visible at  $\Phi \sim 10^{11}n/\text{cm}^2$ . The number of observed hot spots and the noise rate increase after irradiation of  $3 \times 10^9 n/\text{cm}^2$ . No significant changes on the cross talk probability and no significant change on the saturation curves are observed. The main effect is an increase in noise after exposure to high  $n$  dose. Hamamatsu has produced news SiPM/MPPCs with  $20 \mu\text{m} \times 20 \mu\text{m}$  and  $15 \mu\text{m} \times 15 \mu\text{m}$ , which have lower detection efficiency due to more boundaries and thus need a higher bias voltage to compensate for losses. Figure ?? shows the detection efficiency as a function of bias voltage for  $15 \mu\text{m} \times 15 \mu\text{m}$  detectors before and after irradiation. For the new detectors, signal/noise and the equivalent noise charge look fine after irradiation. According to Eugenios study the backward endcap EMC will record  $10^9 n \text{ mm}^2$  after 10 years operation. Thus, if the  $25 \mu\text{m} \times 25 \mu\text{m}$  pixel SiPM/MPPC show a prob-

lem we switch to one of the new SiPM/MPPCs with smaller pixel size.

#### 9.4.2.4 Solid angle, transition to barrel

The backward endcap EMC covers a polar angle region from  $\theta$  to  $\theta$ .

#### 9.4.3 Mechanical design

The 3 mm thick scintillator strips are cut individually from a scintillator plate. Thus, the plate size and the cutting procedure need to be carefully thought through to minimize the amount of waste. For the spiral strips the least waste and fastest production is obtained by fabricating a mould. However, this approach may be too expensive since the total number of spiral strips is rather small. The preferred scintillator material is BC 404 from St Gobain, since it has the smallest decay time for TOF capability and its emission spectrum is reasonably matched to the Y11 absorption spectrum. The strip width is 38 mm at the inner edge increasing to 98 mm at the outer edge. The sides are painted with a white diffuse reflector. Front and back faces are covered with reflectors sheets (3M, Tyvec). To restore uniformity, a pattern of black dots is printed onto the white reflector sheets.

In the center of each strip, a 1.1 mm deep groove is milled into which the 1 mm thick Y11 WLS fiber is inserted. At the outer edge of the strip, the groove is cut a 0.4 mm deeper so that the SiPM/SiPM/MPPC fully covers the fiber. The SiPM/MPPC is housed in a small precisely cut pocket. Especially fabricated fixtures out of Teflon or Nylon will hold a strip. The fiber groove at the outer edge is closed with a plug at the position of the photodetector. The Y11 fiber is pressed against the plug and held with a drop of glue. After removing the plug the SiPM/MPPC is inserted and is glued onto the Y11 fiber to match refractive indices. A mirror is placed at the other end of the fiber to detect the light that moves away from the photodetector. So tolerances in the length of the Y11 fiber are picked up at the mirror end. The strip layout is shown in Figure ??.

To hold the strips in each layer in place 1.5 mm deep and 1 mm wide grooves are cut into the lead plates. The shape of groove matches

Table 9.4: Properties of Hamamatsu MPPCs

MPPC type	# cells 1/mm <sup>2</sup>	C [pF]	R <sub>cell</sub> [kΩ]	C <sub>cell</sub> [fF]	τ = R <sub>c</sub> × C <sub>cell</sub> [ns]	Input [V]	Output [V]	Gain [10 <sup>5</sup> ]
15 μm	4489	30	1690	6.75	11.4	16*8 cables	7.15	2.0
20 μm	2500	31	305	12.4	3.8	67*105	7.15	2.0
25 μm	1600	32	301	20	6.0	72*105	7.15	2.0
50 μm	400	36	141	90	12.7	108+128+96+332 cables	7.15	2.0

that of the strip. A 3 mm thick and 1 m wide and 550 mm long plastic strip is inserted into the groove and is glued. This structure is strong enough to hold the scintillator strips in place. The calorimeter can be rotated by 90°. This is needed for operation with cosmic muons that yield a MIP calibration and allows for testing the calorimeter before installing it into the SuperB detector.

The entire calorimeter just weighs about 1300 Kg. An Al frame with a strong back will hold the EMC backward EC layers. It has several advantages (performance and costs) to build the backward endcap as a single unit. This requires the endcap to slide back on the beam pipe supported on the tunnel walls. It needs to be fixed at the tunnel and is rolled in. Since the inner radius is 31 cm, there is sufficient clearance for pumps and other beam elements. The design of this capability requires a detailed drawing of the beam pipe and the position and size of machine elements.

It is possible, however, to build the backward endcap in two halves with a vertical split. The impact of such a design is that ten strips per layer have to be cut into two segments, where the inner segments have to be read out at the inner radius. This increases the number of channels by 240, requiring 240 additional SiPM/MPPCs, seven extra SPIROC boards and four extra calibration boards. This layout will deteriorate the performance near the vertical boundary. The effect needs to be studied in simulations. This certainly adds extra costs at the order of ~ 20%.

#### 9.4.3.1 Calorimeter construction

#### 9.4.3.2 Support and services

Each SPIROC board has 36\*6 cables one mul-

tiplexed output (USB) to DAQ a low voltage input for +5.5 V and -7.5V a high voltage input for 70V an electronic calibration input an analog output for 23 Each Calibration board has 16\*8 cables 7.15 low voltage for 7.15 7V operating voltage 67\*105 diode output 754 thermocouples per layer 72\*105 cables Total number of cables 108+128+96+332 cables ! 70\*75 100\*0.75m2

#### 9.4.4 SiPM/MPPC readout

The photodetectors are SiPM/MPPCs from Hamamatsu (type ) with a sensitive area of 1 mm × 1 mm holding 1600 pixels with a size of 25 μm × 25 μm. These detectors are avalanche photodiodes operated in the Geiger mode with a bias voltage slightly above the breakdown corresponding to 50 – 70 V providing a gain of a few 10<sup>5</sup>. They are insensitive to magnetic fields. Each pixel typically has a quenching resistor of a few MΩ so they recover within 100 ns. The efficiency is of the order of 10 – 15%. Since the SiPM/MPPCs record single photoelectrons, they are auto-calibrating. They are non-linear requiring non-linearity corrections for higher energies. The dynamic range is determined by the number of pixels. The properties of SiPM/MPPCs are listed in Table 9.4.

A concern with SiPM/MPPCs is radiation hardness. Degradation in performance is observed in studies performed for the SuperB IFR, beginning at integrated doses of order 10<sup>8</sup> 1-MeV-equivalent neutrons/cm<sup>2</sup> [8]. This needs to be studied further, and possibly mitigated with shielding. Another alternative is look into a different photodetector. Recently, Hamamatsu has produced SiPM/MPPCs with pixel sizes of 20 μm × 20 μm and 15 μm × 15 μm (see Table ??). A CMS study shows that the performance of these new photodetector deteriorates only slightly after an irradiation of 10<sup>13</sup>n/cm<sup>2</sup>.

#### 9.4.5 Electronics

The signal of the SiPM/MPPC is first amplified with a charge-sensitive preamplifier then fed into the auto-triggered, bi-gain SPIROC ASIC.

The SPIROC board has 36 channels. Each channel has a variable-gain charge preamplifier, variable shaper and a 12-bit Wilkinson ADC. It allows to measure the charge  $Q$  from one photoelectron (pe) to 2000 pe and the time  $t$  with a 100ps accurate TDC. A high-level state machine is integrated to manage all these tasks automatically and control the data transfer to the DAQ. The SPIROC ASIC was designed to supply the high voltage for the SiPM/MPPC. Using a DAC, individual high voltages within  $\pm 5$  V can be supplied to each photodetector.

The SPIROC ASIC gives Gaussian signals with no tails, shows excellent linearity and low noise. 32 ASIC readout boards are needed to read out the entire endcap. The boards are mounted in two layers behind the endcap. The first layer hold 20 boards and the second layer the remaining 12 boards. Each board connects to 36 SiPM/MPPCs via a ribbon cable that were designed for ILC at a luminosity of  $\mathcal{L} = 10^{34} \text{ cm}^{-2} \text{ s}^{-1}$ .

#### 9.4.6 Calibration

An LED-based calibration system with fixed LED intensities is used to monitor the stability of strip-fiber-SiPM/MPPC system between MIP calibrations, to perform gain calibrations, determine intercalibration constants, and to measure the SiPM/MPPC response functions. This is necessary since the SiPM/MPPCs have a temperature and voltage dependence of the gain

$$\frac{dG}{dT} \sim -1.7\%/K \quad (9.10)$$

$$\frac{dG}{dV} \sim 2.5\%/0.1V \quad (9.11)$$

The temperature and voltage dependence of measuring the charge of the scintillation signal is

$$\frac{dQ}{dT} \sim -4.5\%/K \quad (9.12)$$

$$\frac{dQ}{dV} \sim 7\%/0.1V \quad (9.13)$$

Using the design of the calibration system for the analog hadron calorimeter prototype, the

calibration system is based on an UV LED that couples to 19 clear fibers, of which 18 fibers transfer light to 18 strips and one fiber is read-out by a PIN photodiode to monitor the LED light. Twelve LEDs are mounted on each calibration board. The fibers are routed at the outer edge. They are inserted into a hole in the strip. Thermocouples distributed throughout the outer edge of the endcap measure the temperature which is recorded regularly together with the voltage by a slow control system. After PIN diode correction the stability of LED system is  $< 1\%$ . For the analog hadron calorimeter a study is performed in which one fiber serves several tiles by providing cuts at appropriate positions so that the light is extracted there. If this work it would reduce the number of fibers and calibration boards considerably.

Since the CMB boards are too big to be mounted at the outer radius of the endcap, new boards need to be produced. Using the same concept half-size boards with six LEDs are produced. If each LED couples to 19 fibers, 11 boards are sufficient. They can be mounted in two rings around the endcap. To avoid too small bending radii LEDs from the right ring supply strips to the left and LEDs from the left ring supply strips to the right. So in total, 64 LEDs and 64 PIN diodes are needed.

#### 9.4.7 Backward simulation

Currently there only exists a simple backward EMC model in GEANT4 simulation. The scintillator and the lead are modeled. Each layer is modeled with a complete disc without physical segmentations in  $r$ - $\phi$ . The supporting structure, fibers, electronics, and cables are not modeled yet.

In the fast simulation, the model does not separate lead from scintillator. It uses an artificial material that approximates the overall density, radiation length, interaction length and Moliere radius of the mixture of lead and plastic. The volume is divided into eight rings, each of which is divided into 60 segments. We do not model the logarithmic spirals and lead-scintillator layers to avoid complicated cluster reconstruction and longitudinal shower energy distribution

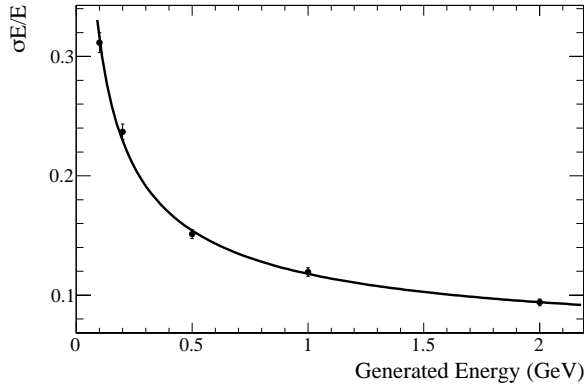


Figure 9.41: The backward EMC energy resolutions,  $\sigma_E/E$ , where  $\sigma_E$  and  $E$  are the Gaussian width and mean in Fig. 9.40, as a function of generated photon energy.

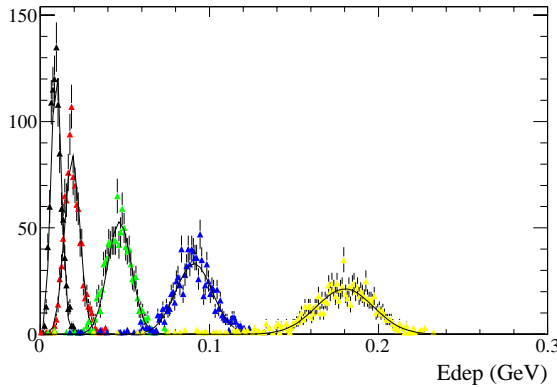


Figure 9.40: Energy depositions in the scintillators of the backward EMC from mono-energetic photons of various energies generated in front of the EMC. See text.

modeling. The energy resolution used in the fast simulation is  $\sigma_E/E = \frac{14\%}{\sqrt{E(\text{GeV})}} \oplus 3\%$ .

#### 9.4.8 Performance in simulations

A GEANT4 simulation is performed to study the energy resolution. We simplify the conditions by ignoring the rest of the detector and shoot mono-energetic photons perpendicular to

the face of the disc. All energy deposited in the scintillator is collected. No clustering algorithm is performed. Figure 9.40 shows the energy deposition of five different energy photons, 100, 200, 500, 1000, and 2000 MeV. On average approximately 9.5% of the photon energy is deposited in the scintillator for 100 MeV photons. This percentage drops to 9.0% for 2 GeV photons.

The energy resolution dependence on generated energy is shown in Fig. 9.41. It can be fitted with the function  $\sigma_E/E = \frac{10\%}{E(\text{GeV})^{0.485}} \oplus 6\%$ .

Fast simulation studies are being performed to investigate the performance gain achieved by the addition of the backward calorimeter. The  $B \rightarrow \tau\nu\tau$  decay presents an important physics channel where hermeticity is a significant consideration. The measurement of the branching fraction has been studied in simulations to evaluate the effect of the backward calorimeter. Events in which one  $B$  decays to  $D^0\pi$ , with  $D^0 \rightarrow K^-\pi^+$ , are used to tag the events, and several of the highest branching fraction one-prong  $\tau$  decays are used.

Besides the selection of the tagging  $B$  decay, and one additional track for the  $\tau$ , the key selection criterion is on  $E_{\text{extra}}$ , the energy sum of all remaining clusters in the EMC. This quantity is used to discriminate against backgrounds by requiring events to have low values; a reasonable criterion is to accept events with  $E_{\text{extra}} < 400$  MeV.

In this study we find that the signal-to-background ratio is improved by approximately 20% if the backward calorimeter is present (Fig. 9.55). The corresponding improvement in precision ( $S/\sqrt{S+B}$ ) for  $75 \text{ ab}^{-1}$  is approximately 8% (Fig. 3.3). We note that only one tag mode has so far been investigated, and this study is ongoing with work on additional modes to obtain results for a more complete sample analysis. Also, the effect of background events superimposed on the physics event has not been fully studied.

Even though the backward EMC is designed to act as a veto device, it can improve the  $\pi^0$  reconstruction efficiency despite the poor energy

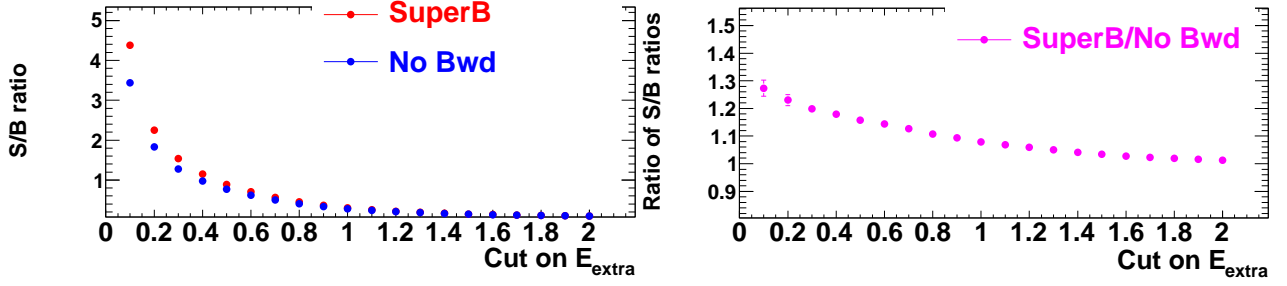


Figure 9.42: Left: Signal-to-background ratio with and without a backward calorimeter, as a function of the  $E_{\text{extra}}$  selection. Right: Ratio of the S/B ratio with a backward calorimeter to the S/B ratio without a backward calorimeter, as a function of the  $E_{\text{extra}}$  selection.

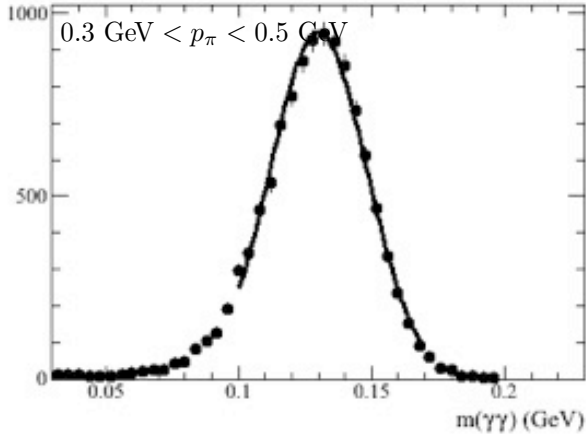


Figure 9.43: Invariant mass resolution of  $\pi^0 \rightarrow \gamma\gamma$  where one photon is detected at the backward EMC.

resolution. The  $\gamma\gamma$  invariant mass resolution where one photon is reconstructed in the backward endcap is around 24 MeV for 200 MeV/c  $\pi^0$  and about 13 MeV at 1 GeV/c (See, e.g., Fig. 9.43).

We test  $B$  reconstruction efficiency using  $B^- \rightarrow D^0\pi^-$  with  $D^0 \rightarrow K^-\pi^+\pi^0$ . Events are separated into two groups. One uses the barrel and forward endcap only; the other includes one photon from the backward EMC with polar angle between  $-0.96 < \cos\theta < -0.89$ . The  $\pi^0$  mass window is 120–145 MeV (100–180 MeV) for the first (second) group. We select  $D^0$  within  $1.830 < m_{K\pi\pi^0} < 1.880$  GeV,

and  $-80 < \Delta E < 50$  GeV for  $B$  candidates. We fit  $m_{\text{ES}}$  distribution to determine the  $B$  reconstruction efficiency. We find that including the backward calorimeter to reconstruct  $\pi^0$  increases the signal efficiency by nearly 4% in this particular channel (Fig. 9.44).

#### 9.4.9 Use for particle identification

Charged particles moving in the backward direction typically have lower momentum. Thus, ionization loss and time-of-flight measurements may provide useful particle identification information, e.g. for  $K/\pi$  separation.

A preliminary study is performed with fast simulation. Single kaons or pions are generated pointed towards the backward endcap. The true arrival time at the first layer is smeared with a Gaussian resolution as the measured time. Using the reconstructed track path length and the measured time, one obtains the velocity. The means and RMSs of the measured velocity distributions for pions and kaons at a given momentum are compared. One can then obtain the  $K/\pi$  separation in terms of  $\sigma$ . This procedure includes uncertainties from momentum measurement and path length reconstruction. For example for 100 ps time resolution, Figure 9.56 shows  $K/\pi$  separation in units of standard deviations as a function of momentum. A separation of more than three standard deviations ( $\sigma$ ) can be achieved for momenta up to 1 GeV/c and approximately  $1.5\sigma$  up to 1.5 GeV/c.

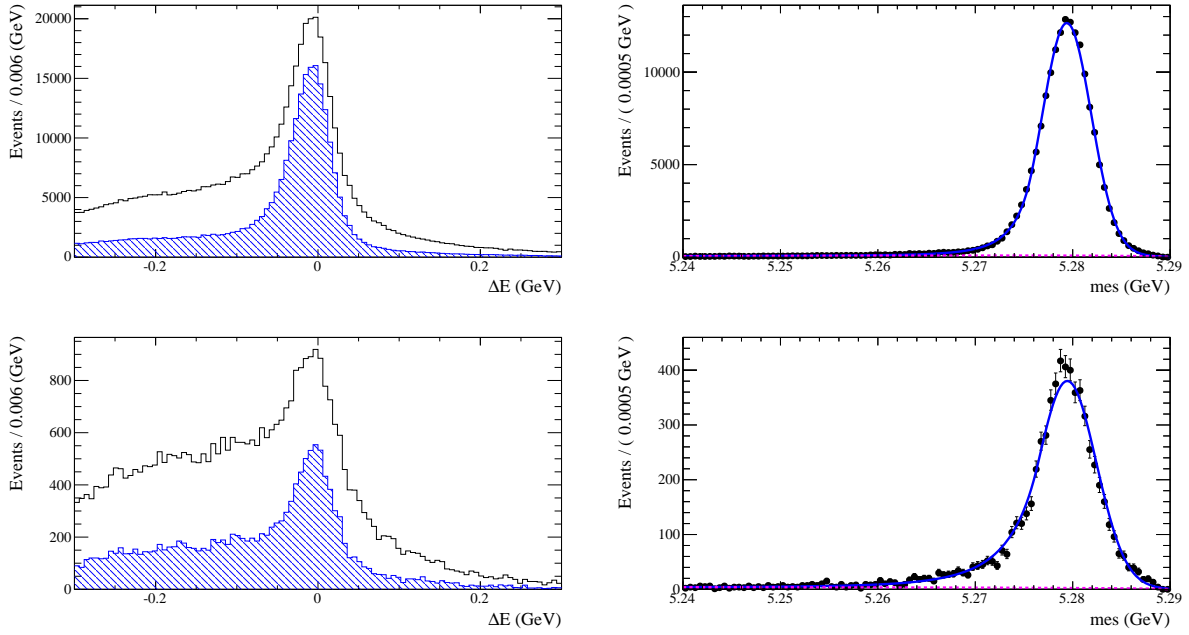


Figure 9.44:  $\Delta E$  (left) and  $m_{ES}$  (right) of  $B^- \rightarrow D^0 \pi^-$  with  $D^0 \rightarrow K^- \pi^+ \pi^0$  reconstruction. Two histograms in each  $\Delta E$  plot are before and after  $D^0$  mass cut. Top: both  $\gamma$ 's are in barrel and forward endcap; bottom: one  $\gamma$  in the backward.

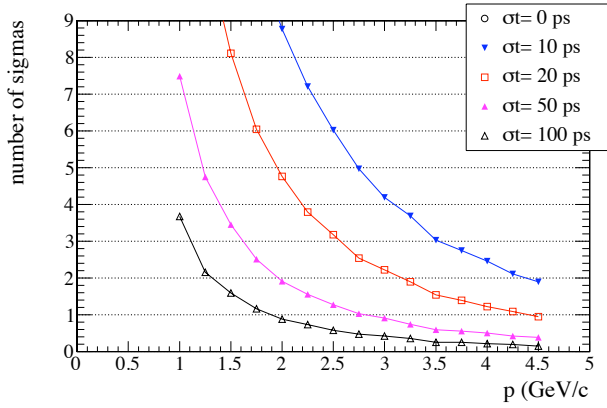


Figure 9.45: Kaon-pion separation versus measured momentum for different timing resolutions in the backward EMC region. The finite separation for perfect timing resolution is because measured momentum is used.

Since each layer measures the time distribution, 24 measurements will be averaged. In addition to timing, the ionization is measured in each layer. For MIP-like particles, the average energy loss per layer is  $dE_{pb} = 4.3$  MeV and  $dE_{sintillator} = 0.6$  MeV. A 0.5 GeV  $\pi$  is at the ionization minimum, while a 0.5 GeV  $K$  is below the minimum. For MIP particles, the ionization loss in the 24 layers is  $\Delta E = 117$  MeV. Since the energy loss below the minimum increases with decreasing momenta as  $1/\beta^2$ ,  $dE/dx$  measurements in the endcap can be combined with the  $dE/dx$  information from the SVT and DCH. Figure ?? shows the ionization curves for  $e, \mu, \pi, K$  and  $p$  as a function of momentum. A  $> 3 \sigma$   $K/\pi$  separation is achievable for momenta up to 0.6 – 0.7 GeV.



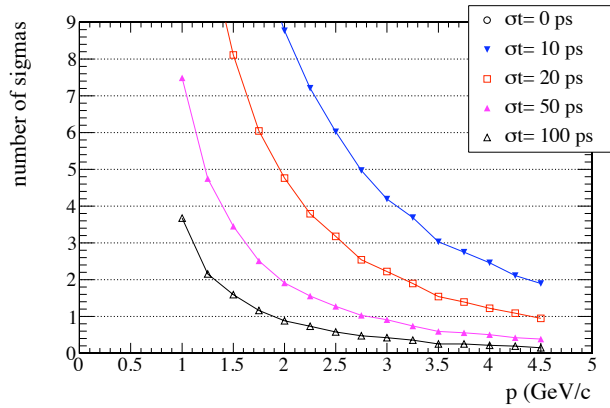


Figure 9.46: Kaon-pion separation versus measured momentum for different time resolutions in the backward EMC region. The finite separation for perfect timing resolution is because measured momentum is used.

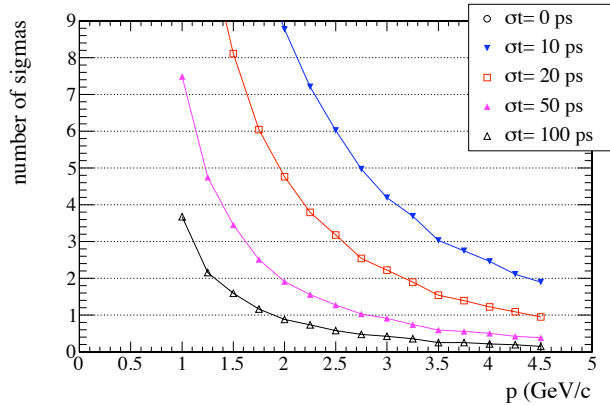


Figure 9.47: Kaon-pion separation versus measured momentum for different time resolutions in the backward EMC region. The finite separation for perfect timing resolution is because measured momentum is used.

#### 9.4.10 Discussion of task force conclusions

### 9.5 Trigger

---

This is a reminder that we need a synopsis of the EMC trigger somewhere in the EMC chapter, although the detailed description will be in the ETD chapter. It is to be determined whether this should be in a separate section or merged with the three sub-calorimeter sections.

#### 9.5.1 Calorimeter readout trigger

##### 9.5.1.1 Normal mode

##### 9.5.1.2 Calibration mode

#### 9.5.2 Calorimeter trigger primitives

### 9.6 Detector protection

---

Personnel ES&H will be elsewhere.

#### 9.6.1 Thermal shock

#### 9.6.2 Mechanical shock, including earthquakes

#### 9.6.3 Fluid spills

#### 9.6.4 Electrical surges, outages

#### 9.6.5 Radiation damage

### 9.7 Cost & Schedule

---

This will appear elsewhere.

#### 9.7.1 WBS structure

#### 9.7.2 Gantt chart

#### 9.7.3 Basis of estimates

#### 9.7.4 Cost and schedule risks



**White Paper text follows, for reference:**

The Super*B* electromagnetic calorimeter (EMC) provides energy and direction measurement of photons and electrons, and is an important component in the identification of electrons versus other charged particles. The system contains three components, shown in Fig. 3.1: the barrel calorimeter, reused from *BABAR*; the forward endcap calorimeter, replacing the *BABAR* forward endcap; and the backward endcap calorimeter, a new device improving the backward solid angle coverage. Table ?? details the solid angle coverage of each calorimeter. The total solid angle covered for a massless particle in the center-of-mass (CM) is 94.1% of  $4\pi$ .

In addition to the *BABAR* simulation for the barrel calorimeter, simulation packages for the new forward and backward endcaps have been developed, both in the form of a full simulation using the Geant4 toolkit and in the form of a fast simulation package for parametric studies. These packages are used in the optimization of the calorimeter and to study the physics impact of different options.

## 9.8 Barrel Calorimeter

The barrel calorimeter for Super*B* is the existing *BABAR* CsI(Tl) crystal calorimeter.[1] Estimated rates and radiation levels indicate that this system will continue to survive and function in the Super*B* environment. It covers  $2\pi$  in azimuth and polar angles from  $26.8^\circ$  to  $141.8^\circ$  in the lab. There are 48 rings of crystals in polar angle, with 120 crystals in each azimuthal ring, for a total of 5,760 crystals. The crystal length ranges from  $16X_0$  to  $17.5X_0$ . They are readout by two redundant PIN diodes connected to a multi-range amplifier. A source calibration system allows calibrating the calorimeter with 6.13 MeV photons from the  $^{16}\text{N}$  decay chain. The *BABAR* barrel calorimeter will be largely unchanged for Super*B*; we indicate planned changes below.

Adding one more ring of crystals at the backward end of the barrel is under consideration. These crystals would be obtained from the current *BABAR* forward calorimeter, that will not be reused in Super*B*. Space is already available for the additional crystals in the existing mechanical structure, although some modification would be required to accommodate the additional readout.

The existing barrel PIN diode readout is kept at Super*B*. In order to accommodate the higher event rate, the shaping time is decreased. The existing “CARE” chip [2] covers the required dynamic range by providing four different gains to be digitized in a ten-bit ADC. However, this system is old, and the failure rate of the analog-to-digital boards (ADBs) is unacceptably high. Thus, a new ADB has been designed, along with a new analog board, the Very Front End (VFE) board, shown in Fig. 9.48. The new design incorporates a dual-gain amplifier, followed by a twelve-bit ADC. In order to provide good least-count resolution on the 6 MeV calibration source, an additional calibration range is provided on the ADB. The existing PIN diodes, with their redundancy, are expected to continue to perform satisfactorily. They are epoxied to the crystals and changing them would be a difficult operation.

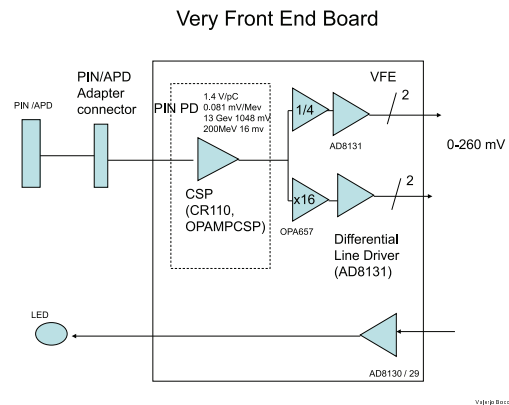


Figure 9.48: Block diagram for the Very Front End board, for the barrel and forward endcap signal readout.

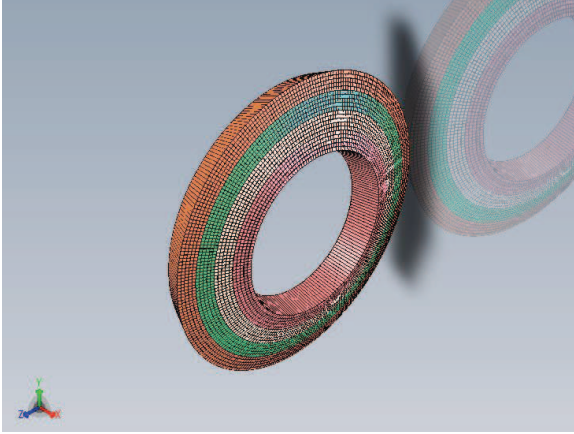


Figure 9.49: Arrangement of the LYSO crystals in groups of rings.

## 9.9 Forward Endcap Calorimeter

The forward electromagnetic calorimeter for SuperB is a new device replacing the BABAR CsI(Tl) forward calorimeter, with coverage starting at the end of the barrel and extending down to  $270\text{ mrad}$  ( $\cos\theta = 0.965$ ) in the laboratory. Because of the increased background levels, a faster and more radiation hard material, such as LYSO or pure CsI, is required in the forward calorimeter. The baseline design is based on LYSO (Lutetium Yttrium Orthosilicate, with Cerium doping) crystals. The advantages of LYSO include a much shorter scintillation time constant (LYSO:  $40\text{ ns}$ , CsI(Tl):  $680\text{ ns}$  and  $3.34\text{ }\mu\text{s}$ ), a smaller Molière radius (LYSO:  $2.1\text{ cm}$ , CsI:  $3.6\text{ cm}$ ), and greater resistance to radiation damage. One radiation length is  $1.14\text{ cm}$  in LYSO and  $1.86\text{ cm}$  in CsI. An alternative choice is pure CsI [3]. However, the light output is much smaller, making LYSO preferable.

There are 20 rings of crystals, arranged in four groups of 5 layers each. The crystals maintain the almost projective geometry of the barrel. Each group of five layers is arranged in modules five crystals wide. The preferred endcap structure is a continuous ring. However, the numbers of modules in each group layers are multiples of

6, allowing the detector to be split in two halves, should that be necessary from installation considerations. The grouping of crystals is summarized in Table 9.5 and illustrated in Fig. 9.49.

Table 9.5: Layout of the forward endcap calorimeter.

Group	Modules	Crystals
1	36	900
2	42	1050
3	48	1200
4	54	1050
Total		4500

Each crystal is up to  $2.5 \times 2.5\text{ cm}^2$  at the back end, with a projective taper to the front. The maximum transverse dimensions are dictated by the Molière radius and by the desire to obtain two crystals from a boule. The length of each crystal is approximately  $20\text{ cm}$ , or  $17.5X_0$ .

### 9.9.1 Mechanical Structure

The support for the crystals is an alveolar structure (*i.e.*, a sort of egg-crate structure, with a cell for each crystal) constructed of either carbon fiber or glass fiber and bounded by two conical structures at the radial extremes. To minimize the dead material between the endcap and the barrel, the outer cone is made of carbon fiber with a thickness between 6 and 10 mm. The inner cone is instead made of 20 to 30 mm-thick aluminum.

With the inclusion of the source calibration system, described below, and the front cooling system, the total front wall thickness may reach 20–30 mm. A good solution that minimizes material in front of the calorimeter is to embed the pipes into the foam core of a sandwich panel completed by two skins of 2–3 mm carbon fiber. A lighter alternative under investigation is to use depressions in pressed aluminum sheets forming the two skins of the front wall to form the calibration and cooling circuits. The support at the back, providing the load-bearing support for the forward calorimeter, is

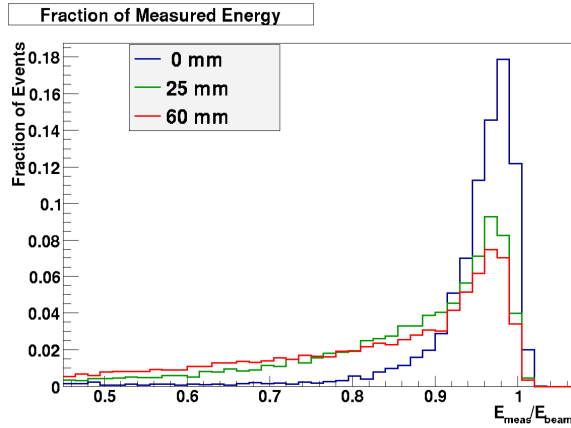


Figure 9.51: Ratio of the measured/beam energy in the forward calorimeter for 100 MeV photons and two different thickness of quartz, as well as no quartz, in front of the calorimeter.

constructed in stainless steel as either an open frame or closed plate.

### 9.9.2 Readout System

Two possible readouts are under study: PIN diodes as used the barrel and APDs (Avalanche Photodiodes). As for the barrel, redundancy is achieved with 2 APDs or PIN diodes per crystal. APDs, with a low-noise gain of order 50, offer the possibility of measuring signals from sub-MeV radioactive sources. This would obviate the need for a step with photomultipliers during the uniformity measurement process during calorimeter construction. A concern in the SuperB environment is the nuclear counter effect from background neutrons. APDs also have an advantage over PIN diodes here. Nevertheless, it may be desirable to use the redundant photodetectors with a comparator arrangement to eliminate spurious large signals due to this background. This is under investigation. The disadvantage of APDs is the gain dependence on temperature, which can be of order  $2\%/^{\circ}\text{C}$  (e.g. [4]). This requires tight control of the readout temperature. The same electronics as for the barrel

is used, with an adjustment to the VFE board gain with the APD choice.

### 9.9.3 Calibration and Beam Test

The source calibration system is a new version of the 6.13 MeV calibration system already used in BABAR. This system uses a neutron generator to produce activated  $^{16}\text{N}$  from fluorine in Fluorinert [5] coolant. The activated coolant is circulated near the front of the crystals in the detector, where the  $^{16}\text{N}$  decays with a 7 s half-life. The 6.13 MeV photons are produced in the decay chain  $^{16}\text{N} \rightarrow ^{16}\text{O}^* + \beta$ ,  $^{16}\text{O}^* \rightarrow ^{16}\text{O} + \gamma$ .

Two beam tests are planned to study the LYSO performance and the readout options. The first beam test is at Frascati's Beam Test Facility, covering the 50–500 MeV energy range. The second beam test is at CERN, to cover the GeV energy range. In addition, a prototype alveolar support structure is being constructed for the beam test.

### 9.9.4 Performance Studies

Simulation studies are underway to optimize the detector configuration. It is important to use a realistic clustering algorithm in these studies, since in actual events multiple particles can overlap, requiring clever pattern recognition. Fig. 9.50 shows how the measured energy distribution changes for different reconstruction algorithms.

Particular attention has been devoted to the study of the effect of material in front of the forward calorimeter, for instance due to a proposed forward PID device. Material in front of the calorimeter enhances the low-energy tail of the measurement, although peak width measures, such as the FWHM, are almost unaffected, as shown in Fig. 9.51. for the cases of 25 and 60 mm of quartz in front of the calorimeter.

A more meaningful measure that we may use is:

$$f_{90} \equiv \frac{E_{\text{true}} - E_{90}}{E_{\text{true}}},$$

where  $E_{\text{true}}$  is the energy of the generated photon and  $E_{90}$  gives the 90% quantile of the measured energy distribution, *i.e.*, 90% of measurements of the photon energy are above this value.

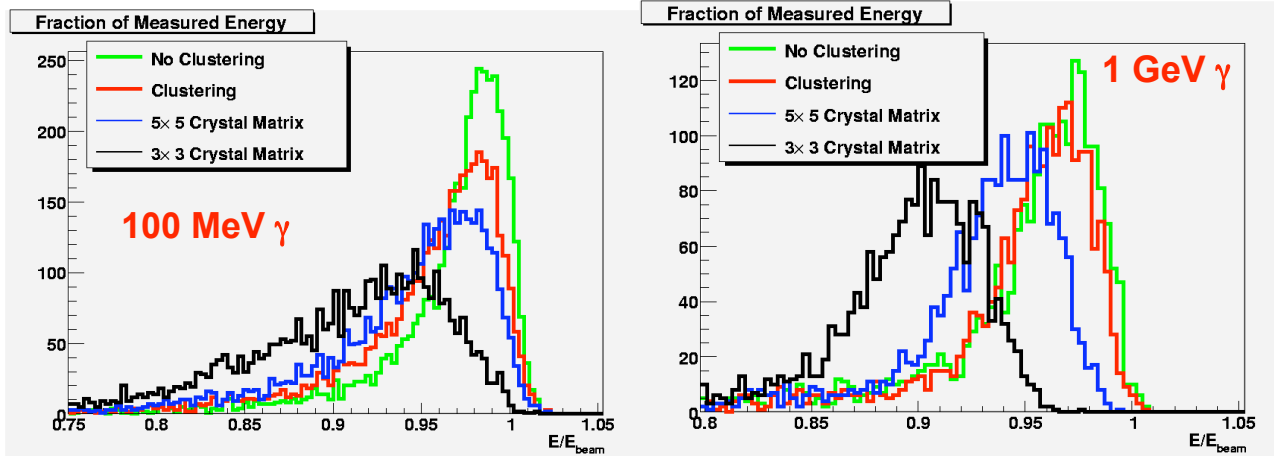


Figure 9.50: Effect on the measured energy distribution for various reconstruction algorithms. The “No clustering” distribution results from simply adding all crystal energies greater than 1 MeV. The “Clustering” distribution results from the algorithm used in *BABAR*. The curves labeled  $5 \times 5$  crystal matrix and  $3 \times 3$  crystal matrix are simple sums of energy deposits in 25 or 9 crystals, respectively, centered on the crystal with the most energy. Left: 100 MeV photons; Right: 1 GeV photons.

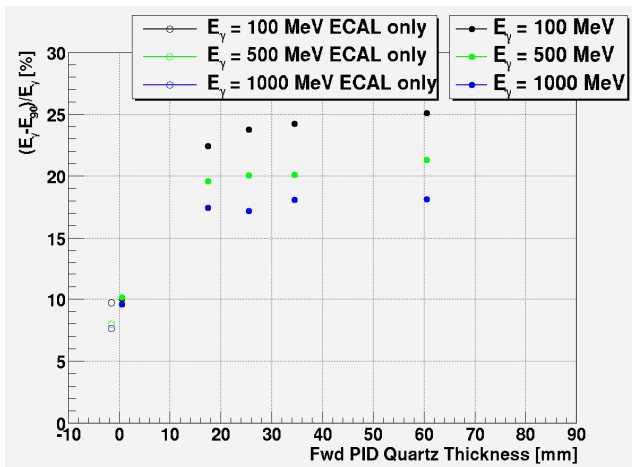


Figure 9.52: The effect of quartz material in front of the forward calorimeter, as a function of thickness and photon energy. The ordinate is  $f_{90}$ , explained in the text, expressed as per cent.

Fig. 9.52 shows the effect on the  $f_{90}$  measure of resolution as a function of the quartz thickness.

Ideally, the transition between the barrel and forward calorimeters should be smooth, in order to contain the electromagnetic showers and to keep pattern recognition simple. Some possibilities for particle identification however require the forward calorimeter to be moved back from the IP relative to the smooth transition point. The effect of this on photon energy resolution has been studied, see Fig. 9.53. The resolution degrades in the barrel-endcap transition region as expected, but there is substantially no dependence on the  $z$ -position.

## 9.10 Backward Endcap Calorimeter

The backward electromagnetic calorimeter for SuperB is a new device with the principal intent of improving hermeticity at modest cost. Excellent energy resolution is not a requirement, since there is significant material from the drift chamber in front of it. Thus a high quality crystal calorimeter is not planned for the backward region. The proposed device is based on a

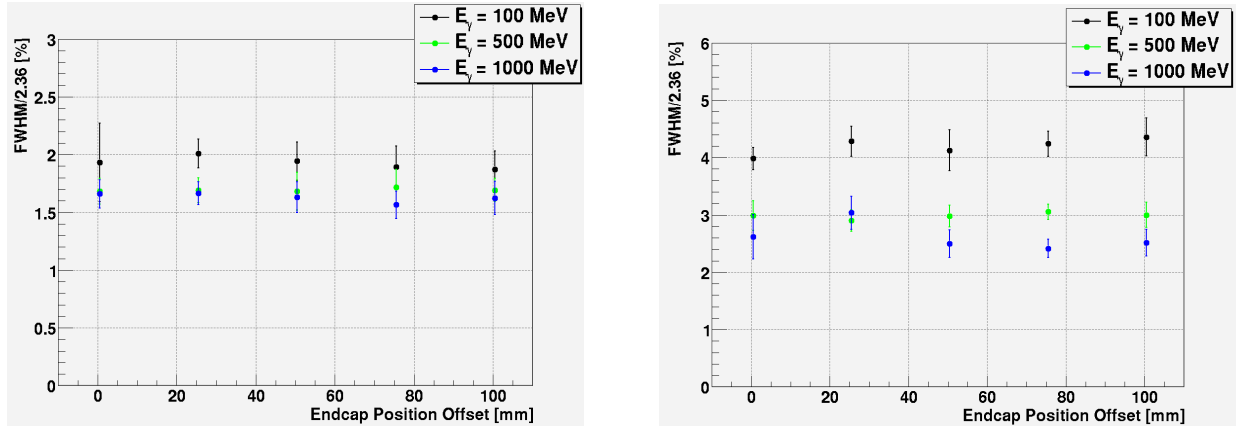


Figure 9.53: Effect on resolution of z-position of forward calorimeter. Left: Resolution as a function of position for showers away from the edges of the forward calorimeter. Right: Resolution as a function of position for showers in the transition region between the barrel and forward calorimeters. Note the different scales.

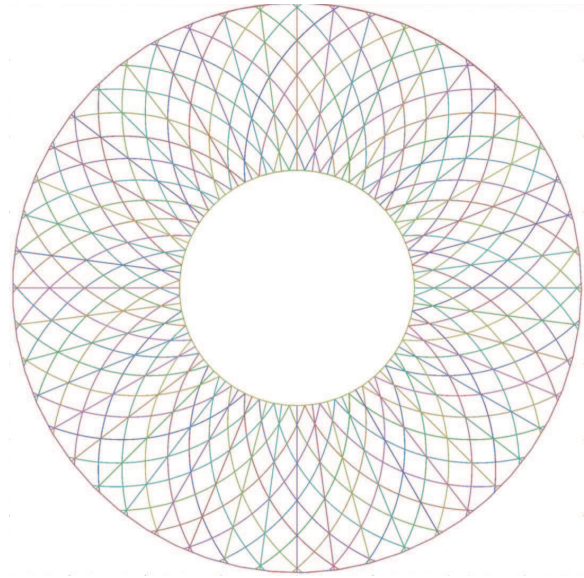


Figure 9.54: The backward EMC, showing the scintillator strip geometry for pattern recognition.

multi-layer lead-scintillator stack with longitudinal segmentation providing capability for  $\pi/e$  separation.

The backward calorimeter is located starting at  $z = -1320$  mm, allowing room for the drift chamber front end electronics. The inner radius is 310 mm, and the outer radius 750 mm. The

total thickness is  $12X_0$ . It is constructed from a sandwich of 2.8 mm Pb alternating with 3 mm plastic scintillator (*e.g.*, BC-404 or BC-408). The scintillator light is collected for readout in wavelength-shifting fibers (*e.g.*, 1 mm Y11).

To provide for transverse spatial shower measurement, each layer of scintillator is segmented into strips. The segmentation alternates among three different patterns for different layers:

- Right-handed logarithmic spiral;
- Left-handed logarithmic spiral; and
- Radial wedge.

This set of patterns is repeated eight times to make a total of 24 layers. With this arrangement, the fibers all emerge at the outer radius of the detector. There are 48 strips per layer, for a total of 1152 strips. The strip geometry is illustrated in Fig. 9.54

It is desirable to maintain mechanical integrity by constructing the scintillator layers with several strips from a single piece of scintillator, and not completely severing them. Isolation is achieved by cutting grooves at the strip boundaries. The optimization of this with respect to cross-talk and mechanical properties is under investigation.



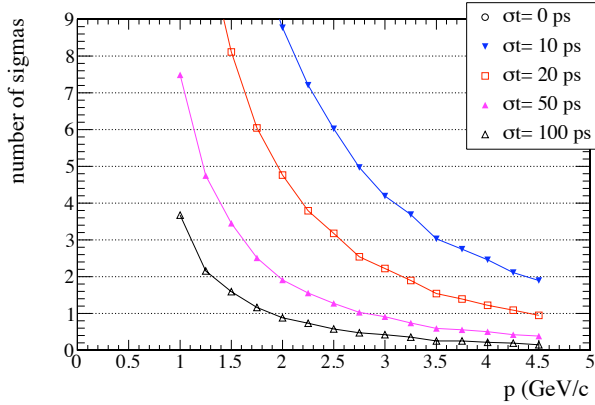


Figure 9.56: Kaon-pion separation versus measured momentum for different timing resolutions in the backward EMC region. The finite separation for perfect timing resolution is because measured momentum is used.

The readout fibers are embedded in grooves cut into the scintillator. Each fiber is read out at the outer radius with a  $1 \times 1 \text{ mm}^2$  multi-pixel photon counter (MPPC, or SiPM, for “silicon photomultiplier”) [6]. A mirror is glued to each fiber at the inner radius to maximize light collection. The SPIROC (SiPM Integrated Read-Out Chip) integrated circuit [7] developed for the ILC is used to digitize the MPPC signals, providing both TDC (100 ps) and ADC (12 bit) capability. Each chip contains 36 channels.

A concern with the MPPCs is radiation hardness. Degradation in performance is observed in studies performed for the SuperB IFR, beginning at integrated doses of order  $10^8$  1-MeV-equivalent neutrons/ $\text{cm}^2$  [8]. This needs to be studied further, and possibly mitigated with shielding.

Simulation studies are being performed to investigate the performance gain achieved by the addition of the backward calorimeter. The  $B \rightarrow \tau \nu_\tau$  decay presents an important physics channel where hermeticity is a significant consideration. The measurement of the branch-

ing fraction has been studied in simulations to evaluate the effect of the backward calorimeter. Events in which one  $B$  decays to  $D^0 \pi$ , with  $D^0 \rightarrow K^- \pi^+$ , are used to tag the events, and several of the highest branching fraction one-prong  $\tau$  decays are used.

Besides the selection of the tagging  $B$  decay, and one additional track for the  $\tau$ , the key selection criterion is on  $E_{\text{extra}}$ , the energy sum of all remaining clusters in the EMC. This quantity is used to discriminate against backgrounds by requiring events to have low values; a reasonable criterion is to accept events with  $E_{\text{extra}} < 400 \text{ MeV}$ .

In this study we find that the signal-to-background ratio is improved by approximately 20% if the backward calorimeter is present (Fig. 9.55). The corresponding improvement in precision ( $S/\sqrt{S+B}$ ) for  $75 \text{ ab}^{-1}$  is approximately 8% (Fig. 3.3). We note that only one tag mode has so far been investigated, and this study is ongoing with work on additional modes to obtain results for a more complete sample analysis. Also, the effect of background events superimposed on the physics event has not been fully studied.

The possibility of using the backward end-cap for particle identification as a time-of-flight measuring device is also under investigation. Figure 9.56 shows, for example, for 100 ps timing resolution, a separation of more than three standard deviations ( $\sigma$ ) can be achieved for momenta up to  $1 \text{ GeV}/c$  and approximately  $1.5\sigma$  up to  $1.5 \text{ GeV}/c$ .

## 9.11 R&D

### 9.11.1 Barrel Calorimeter

The main R&D question for the barrel concerns the shaping time. Simulation work is underway to investigate pile-up effects from backgrounds. In addition, electronics and software issues connected with the possibility of adding one more ring of CsI crystals at the back end are still to be addressed.

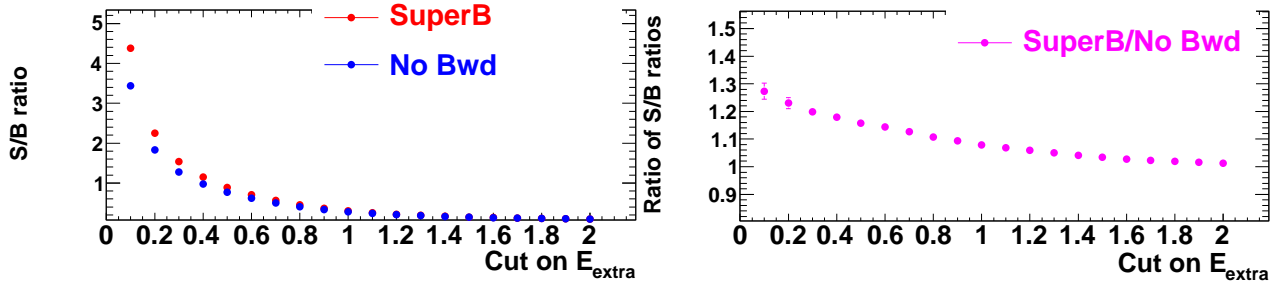


Figure 9.55: Left: Signal-to-background ratio with and without a backward calorimeter, as a function of the  $E_{\text{extra}}$  selection. Right: Ratio of the S/B ratio with a backward calorimeter to the S/B ratio without a backward calorimeter, as a function of the  $E_{\text{extra}}$  selection.

### 9.11.2 Forward Calorimeter

The forward calorimeter is a new device, and we are planning for two beam tests are planned to test the performance of an LYSO crystal array as well as the solutions for the electronics and mechanical designs. The beam tests will also investigate the use of PIN diodes and APDs as readout options as well as the effect of material in front of the crystals in the beam test. Simulation work is ongoing to predict performance and backgrounds. Possible modifications to the electronics design to deal with neutron nuclear-counter signals in the photodetector will be investigated. There is an ongoing R&D effort with vendors to produce crystals with good light output and uniformity at an acceptable cost. The crystal support and integration of the calibra-

tion and cooling circuits with the mechanical structure is under investigation in consultation with vendors.

### 9.11.3 Backward Calorimeter

A beam test of the backward calorimeter is also planned, probably concurrent with the forward calorimeter beam test at CERN. The mechanical support and segmentation of the plastic scintillator is being investigated for a solution that achieves simplicity and acceptable cross-talk. The use of multi-pixel photon counters is being studied, including the radiation damage issue. The timing resolution for a possible time-of-flight measurement is an interesting question. Further simulation studies are being made to characterize the performance impact of the backward calorimeter.





# Bibliography

- [1] B. Aubert *et al.* (BABAR Collaboration), *The BABAR Detector*, Nucl. Instrum. Methods Phys. Res., Sect. A **479**, 1 (2002) [arXiv:hep-ex/0105044].
- [2] G. Haller and D. Freytag, IEEE Trans. Nucl. Sci. **43**, 1610 (1996).
- [3] I. Nakamura, *Belle Electromagnetic Calorimeter and its sBelle Upgrade*, J. Phys. Conf. Ser. **169**, 012003 (2009).
- [4] CMS ECAL Technical Design Report, CERN/LHCC 97-33 (1997), [http://cms-ecal.web.cern.ch/cms-ecal/ECAL\\_TDR/ref/C4\\_P107-116.pdf](http://cms-ecal.web.cern.ch/cms-ecal/ECAL_TDR/ref/C4_P107-116.pdf).
- [5] Fluorinert is the trademark name for polychlorotrifluoro-ethylene), manufactured by 3M Corporation, St. Paul, MN, USA.
- [6] Hamamatsu S10362-11 series MPPC, [http://jp.hamamatsu.com/resources/products/ssd/pdf/s10362-11series\\_kapd1022e05.pdf](http://jp.hamamatsu.com/resources/products/ssd/pdf/s10362-11series_kapd1022e05.pdf).
- [7] M. Bouchel, *et al.*, *SPIROC (SiPM Integrated Read-Out Chip): Dedicated very front-end electronics for an ILC prototype hadronic calorimeter with SiPM read-out*, NSS '07 IEEE **3**, 1857 (2007).
- [8] M. Angelone *et al.*, *Silicon Photo-Multiplier radiation hardness tests with a beam controlled neutron source*, arXiv:1002.3480 [physics.ins-det].